Synaptic Input Variation Enhances Rate Coding at the Expense of Temporal Precision in Cochlear Nucleus Neurons

(Abbreviated title): Synaptic Input Variation in Globular Bushy Cells

Chunjian Wang[1,2], Go Ashida[3,4], Christian Keine[1,2], Ivan Milenkovic[1,2,4]

[1]Department for Human Medicine, Carl von Ossietzky Universität Oldenburg, Germany
[2]Research Center Neurosensory Science, Carl von Ossietzky Universität Oldenburg, Germany
[3]Department for Neuroscience, Carl von Ossietzky Universität Oldenburg, Germany
[4]Cluster of Excellence "Hearing4all", Carl von Ossietzky Universität Oldenburg, Germany

ORCIDs:

Chunjian Wang: 0000-0002-3399-3489
Go Ashida: 0000-0002-8886-1213
Christian Keine: 0000-0003-0995-9667
Ivan Milenkovic: 0000-0003-1431-9031

Abstract

Synaptic convergence is fundamental to neuronal circuit function, underpinning computations such as coincidence detection and signal integration. Across sensory systems, convergence architecture and synaptic input strengths are key for extracting stimulus features and processing of sensory information. In the cochlear nucleus, globular bushy cells (GBCs) receive convergent inputs from multiple auditory nerve fibers via large endbulb of Held terminals. While these inputs vary considerably in size, even among those targeting the same cell, the functional consequences of this variation for sound encoding remain unclear. Here, we investigated how synaptic input variation shapes sound encoding in GBCs of Mongolian gerbils using *in vitro* conductance-clamp recordings and computational modeling. By simulating synaptic inputs with variable strength distributions, we found that increasing input variation enhances rate coding at the expense of temporal precision. These findings suggest that endbulb strength heterogeneity allows the GBC population to operate along a functional continuum, generating diverse information streams to downstream targets.

Keywords: Cochlear nucleus; globular bushy cells; temporal precision; endbulb of Held; coincidence detection; conductance-clamp; auditory nerve; Mongolian gerbil; auditory brainstem; functional heterogeneity; computational modeling

Introduction

Neuronal circuits process information through intricate patterns of synaptic communication. A fundamental principle governing these circuits is synaptic convergence, where individual neurons integrate signals from multiple presynaptic sources. The degree of convergence varies widely across cell types and brain regions, reflecting adaptations to circuit-specific computational demands.

This principle is particularly evident in sensory systems, where parallel pathways often specialize in extracting distinct stimulus features [1–5]. For example, the auditory brainstem exhibits a broad spectrum of synaptic convergence. At one extreme, neurons in the medial nucleus of the trapezoid body (MNTB) are driven by a single large axosomatic terminal, the calyx of Held, which ensures fast and reliable signal transmission [6–11]. In contrast, octopus and D-stellate cells in the cochlear nucleus (CN) integrate signals from dozens of auditory nerve (AN) fibers, responding selectively to the coincident firing of their inputs [12–16]. Even within a single cell type, convergence can differ by orders of magnitude: primate retinal ganglion cells in the fovea receive input from only a few bipolar cells, whereas those in the periphery integrate signals from hundreds of inputs [17–19]. In the nucleus magnocellularis, the avian CN homolog, synaptic convergence is tightly aligned with functional demands: neurons tuned to low frequencies receive numerous small inputs, whereas high-frequency neurons are contacted by fewer, larger terminals to optimize temporal processing [20,21]. Together, these examples illustrate how convergence patterns are finely tuned to the functional requirements of a circuit.

Beyond the sheer number of inputs, variation in synaptic strength among converging inputs represents another critical, yet less understood, factor in neuronal circuit function [22–26]. Across diverse brain regions, including the cerebellum, thalamus, and cortex, some neurons integrate many weak subthreshold inputs, while others are dominated by one or two suprathreshold “driver” inputs alongside multiple weaker ones [22,23,26–28]. Understanding

how this variation in synaptic strength shapes neuronal processing is essential for deciphering the computational principles of sensory signaling.

In this study, we investigated globular bushy cells (GBCs) in the mammalian CN as a model system to explore the functional impact of synaptic input variation. Located near the AN root in the anteroventral (AVCN) and posteroventral cochlear nucleus (PVCN) [29,30], GBCs receive excitatory inputs from multiple AN fibers via large presynaptic terminals known as endbulbs of Held. The number of inputs ranges from 5 to 12 in mice [14,31] to over 20 in cats [32–35]. Functionally, GBCs are essential for high-fidelity temporal processing of auditory signals and often exhibit greater temporal precision than their AN inputs [1,36,37]. Recent morphological analyses have revealed considerable heterogeneity in the size of endbulbs contacting individual GBCs. While some GBCs receive inputs from many similarly sized, subthreshold endbulbs, others are innervated by a few large, suprathreshold endbulbs alongside smaller ones [31,38]. Despite this documented morphological heterogeneity, the computational implications for GBC sound processing remain unclear.

To address this knowledge gap, we combined *in vitro* whole-cell conductance-clamp recordings from GBCs in Mongolian gerbils with computational modeling. By simulating varying degrees of heterogeneity among AN inputs, we assessed the impact of this variation on GBC firing rates and temporal precision. Our results demonstrate that the degree of input variation critically shapes GBC output. Specifically, increasing variation elevates firing rates at the cost of temporal precision in encoding stimulus fine structure. These findings suggest that morphological diversity among endbulb inputs is a key parameter determining GBC encoding strategy, thereby regulating the auditory cues delivered to downstream sound-localization circuits.

Results

Synaptic input variation enhances GBC firing but reduces temporal precision

To study the impact of synaptic input variation, we targeted GBCs based on their well-established anatomical and electrophysiological characteristics. Located in the caudal AVCN near the AN root and PVCN [29], GBCs are characterized by round-to-oval cell bodies with few short dendrites (Fig. 1A1). Electrophysiologically, GBCs fire one or a few action potentials (APs) in response to suprathreshold current injection and exhibit low input resistance (45.5 ± 18 MΩ) and a fast membrane time constant (1.1 ± 0.6 ms, n = 70) at rest (Fig. 1A2). In response to low-frequency sounds, GBCs sustain firing rates up to several hundred spikes per second, with APs temporally aligned to the stimulus fine-structure [36,37,39].

Using an established model of the auditory periphery [40], we simulated independent spike trains for 10 convergent AN fibers responding to 200-ms pure tones (10 repetitions) at frequencies of 350 Hz, 1 kHz, and 3.5 kHz. These frequencies were selected to capture the range where AN fibers exhibit robust phase-locking (350 Hz and 1 kHz) up to the limit where phase-locking declines in rodents (3.5 kHz) [37,39]. The resulting AN spike trains were then convolved with an experimentally derived EPSC waveform to create conductance trains, which were injected into recorded GBCs. By systematically varying the synaptic input strength distribution across these 10 simulated AN fibers, we defined three distinct conditions: ‘no variation’ (all inputs of equal strength: coefficient of variation v = 0), ‘medium variation’ (v = 0.4), and ‘high variation’ (v = 1) (Fig. 1B). In the ‘high variation’ condition, the largest input was near or above spike threshold, while for the ‘no’ and ‘medium’ variation conditions, all inputs remained subthreshold.

First, we analyzed how input variation impacted firing rates and observed a frequency-dependent effect. At stimulation frequencies of 1.0 and 3.5 kHz, increasing input variation elevated average GBC firing rates (1 kHz: ‘no variation’ = 135 ± 49 Hz vs. ‘high

variation' = 175 ± 35 Hz, p = 7.9e-6, n = 15). In contrast, during 350 Hz stimulation, firing rates decreased slightly under 'high variation' ('no variation' = 251 ± 53 Hz vs. 'high variation' = 234 ± 40 Hz, p = 0.01, Fig. 1C1). These changes were uncorrelated with the cells' input resistance (r_s = -0.13, p = 0.68) or membrane time constant (r_s = 0.13, p = 0.67).

Next, we assessed temporal precision using vector strength (VS) [41]. Simulated AN inputs exhibited VS values of 0.75 at 350 Hz and 0.77 at 1000 Hz, consistent with *in vivo* observations [42–45]. Postsynaptically, GBCs showed robust phase-locking at 350 Hz and 1 kHz, but not at 3.5 kHz, aligning with previous data [37]. Notably, increasing input variation significantly reduced phase-locking, particularly at 350 Hz (main effect variation: p = 3.7e-6; 350 Hz: 'no variation' = 0.86 ± 0.02 vs. 'high variation' = 0.81 ± 0.01, p = 3.3e-8, Fig. 1C2). Similar to firing rates, the reduction in VS was independent of input resistance (r_s = -0.31, p=0.3) or membrane time constant (r_s = -0.16, p = 0.59). Together, these results indicate a trade-off whereby higher input variation increases firing rates at the cost of low-frequency phase-locking.

Effects of input variation are well reproduced in a coincidence-counting model

To determine whether these experimental observations can be generalized and arose primarily from input statistics, we employed a computational GBC model, originally developed for cats and adapted for gerbils [4]. In this model, an output spike is generated when the summed inputs exceed an adaptive threshold (see Methods). We drove the model with simulated AN spike trains identical to those used in our *in vitro* experiments, testing a wide range of input variations, including the 'no', 'medium', and 'high' variations from our conductance-clamp recordings (Fig. 2A). The model faithfully reproduced the key experimental findings of increased firing rates (Fig. 2B) and reduced vector strength with higher input variation (Fig. 2C). This suggests that the interaction between synaptic input statistics and a simplified cellular integration mechanism is sufficient to replicate the experimentally observed phenomena.

Higher synaptic input variation impacts AP latency and increases temporal jitter

Given that increased synaptic input variation enhances overall firing rates (Fig. 1C1), we next investigated its impact on the onset and sustained phases of GBC responses. To isolate these epochs, we constructed peristimulus time histograms (PSTH) from responses to a 3.5 kHz pure-tone, a frequency selected to minimize confounding phase-locking effects. Consistent with *in vivo* recordings [1,46–48], both simulated AN inputs and GBC responses displayed primary-like PSTHs characterized by a sharp onset peak followed by adaptation to a lower sustained rate (Fig. 3A). Additionally, GBC PSTHs displayed the characteristic 'notch' immediately following the onset peak. Quantitative analysis confirmed that input variation affected response epochs differently. While 'high variation' significantly reduced onset spike probability ('no variation' = 0.97 ± 0.02 vs. 'high variation' = 0.94 ± 0.02, p = 7.3e-5, n = 17, Fig. 3B2) it increased both sustained firing rates and spontaneous activity (sustained: 'no variation' = 72 ± 27 Hz vs. 'high variation' = 131 ± 28 Hz, p = 3.2e-11, Fig. 3B3; spontaneous: 'no variation' = 25 ± 14 Hz vs. 'high variation' = 65 ± 15 Hz, p = 4.9e-11, Fig. 3B4).

To probe the timing of the response onset, we analyzed the minimum first-spike latency (FSL_{min}) and jitter. Because high spontaneous rates can lead to an apparent decrease in latency, we used a method that accounts for differences in baseline firing [49]. This revealed a nuanced result, with FSL_{min} slightly but significantly prolonged in the 'high variation' condition (Fig. 3B5, 'no variation' = 2.83 ± 0.11 ms vs. 'high variation' = 2.88 ± 0.09 ms, p = 4.5e-4). While first-spike jitter in GBCs was generally lower compared to their AN input, it significantly increased with higher input variation (Fig. 3B6, 'no variation' = 0.22 ± 0.02 ms vs. 'high variation' = 0.27 ± 0.02 ms, p = 1.6e-9). The computational model replicated those findings (Fig. 3C), reproducing the characteristic PSTH shapes (Fig. 3A3) and the gradual change of firing rates with input variation. The model offered further insight into spontaneous rates, revealing a sharp increase at input variations of 0.7-0.8 (Fig. 3C4), corresponding to the transition point where the largest input became suprathreshold. Although the model also captured the increases in FSL_{min} and first-spike jitter (Fig. 3C5, 3C6), the simulated

distributions were narrower than the experimental data, likely reflecting the absence of biological noise sources (e.g., channel and thermal fluctuations). In summary, both experimental and modeling results demonstrated that input variation differentially sculpts GBC responses by enhancing sustained firing rates while simultaneously degrading both the reliability and temporal precision of the response onset.

Input variation modulates GBC encoding of amplitude-modulated sounds

The results from pure-tone stimulation suggested a trade-off where low input variation favors high temporal precision, while high input variation enhances firing rates. To further explore this phenomenon in the context of more complex, naturalistic stimuli, we examined GBC responses to sinusoidal amplitude-modulated (SAM) sounds, which capture the temporal fluctuations present in speech and environmental sounds [50–52]. Effective SAM encoding requires both precise spike timing relative to the modulation cycle (temporal code) and the ability of firing rates to track changes in sound level (rate code). GBCs are known to effectively follow rapid amplitude modulations [53–55].

We simulated the spiking responses of AN fibers to a 13 kHz tonal carrier, 100% amplitude-modulated at frequencies of 200, 600, and 2000 Hz. Consistent with previous in vivo observations [56,57], AN responses exhibited envelope phase-locking for 200 and 600 Hz. Injecting these conductance trains into GBCs under the ‘no’, ‘medium’, and ‘high variation’ conditions yielded robustly modulated firing rates (Fig. 4A2), a result faithfully reproduced by the GBC model (Fig. 4A3). In both the experimental data and the model, responses appeared sharper and more temporally restricted under the ‘no variation’ condition compared with the ‘high variation’ condition.

Consistent with pure-tone data, overall firing rates during SAM stimulation increased significantly with input variation across all modulation frequencies (main effect of variation: $p = 3e\text{-}10$; 600 Hz: ‘no variation’ = 67 ± 50 Hz vs. ‘high variation’ = 115 ± 38 Hz, $p = 1.5e\text{-}7$, n

= 15, Fig. 4B1). Next, we assessed temporal coding fidelity using two complementary metrics: VS and correlation index (CI). The VS indicated robust phase-locking for 200 Hz and 600 Hz but decreased significantly with higher input variation (main effect of variation: p =5.7e-14, 600 Hz**:** **‘**no variation’ = 0.51 ± 0.06 vs. ‘high variation’ = 0.37 ± 0.03, p = 7.2e-10, Fig. 4B2). This is consistent with the reduced VS observed during pure-tone stimulation, indicating weaker encoding of the modulation fine-structure. Similarly, the CI, which quantifies spike time precision across stimulus repetitions [58,59], decreased significantly with higher input variation (main effect of variation: p =5.9e-13; 600 Hz: **‘**no variation’ = 1.53 ± 0.12 vs. ‘high variation’ = 1.26 ± 0.04, p = 3e-8, Fig. 4B3). Together, these measures indicate that increased input variation reduces both phase-locking to the modulation cycle and spike time consistency across trials. In contrast, entrainment index increased significantly with input variation at low modulation frequencies (main effect of variation: p =4.7e-6, 200 Hz: ‘no variation’ = 0.6 ± 0.17 vs. ‘high variation’ = 0.68 ± 0.1, p = 0.005, Fig. 4B4). At 200 Hz, the distributions of the measured and simulated entrainment index were broader than those of the vector strength (Fig 4B2), likely because entrainment depends on firing rate, which was broadly distributed (Fig 4B1), whereas phase-locking (measured by VS) is independent from the spike rate.

Next, we investigated how well GBC firing rates tracked the stimulus envelope, reflecting their rate-coding capacity. Normalized cross-correlation ($Corr_{Norm}$) revealed that firing rates tracked the stimulus envelope more effectively under ‘high variation’ (main effect of variation: p=1.8e-10; 200 Hz**:** **‘**no variation’ = 0.87 ± 0.02 vs. ‘high variation’ = 0.93 ± 0.01, p = 2.5e-10, Fig. 4B5). In summary, during SAM stimulation, increased input variation shifts the GBC coding strategy by degrading fine-structure temporal precision (Figs. 1C2, 2C) while simultaneously improving envelope representation through firing rate modulation. This suggests that GBCs receiving different convergent patterns of AN inputs might be differentially suited to either favor precise temporal representation, requiring highly coincident inputs, or emphasize envelope tracking via firing rate modulation and generally higher firing rates [60–62].

Impact of input variation is consistent with morphologically plausible input sizes

Our results suggest that input variation shifts the operational focus of GBCs between temporal precision (coincidence detection) and firing rate encoding. To determine if this principle arises directly from the known anatomical diversity, we next generated synaptic input variations constrained by morphological measurements of mouse GBCs [31]. From these measurements, we derived two conditions approximating the variance of our previous 'medium' ($v \approx 0.33$, $morph_{MED}$) and 'high' ($v \approx 0.8$, $morph_{HIGH}$) conditions.

GBC responses to pure tones under morphologically constrained input variations were in line with our previous observations. Consistent with the shift towards rate coding, the $morph_{HIGH}$ condition yielded significantly higher firing rates at 1 kHz and 3.5 kHz stimulation frequencies (1 kHz: $morph_{MED}$ = 88 ± 27 Hz vs. $morph_{HIGH}$ = 114 ± 32 Hz, p = 4.2e-9, n = 17, Fig. 5A). Concurrently, VS at 350 Hz and 1 kHz was significantly reduced under high input variation (1 kHz: $morph_{MED}$ = 0.65 ± 0.04 vs $morph_{HIGH}$ = 0.62 ± 0.05, p = 5.3e-5, Fig. 5B). Analysis of onset responses revealed that $morph_{HIGH}$ prolonged FSL_{min} (3.5 kHz: $morph_{MED}$ = 2.84 ± 0.07 ms vs. $morph_{HIGH}$ = 2.91 ± 0.07, p = 5.3e-7, Fig. 5C) and increased temporal jitter (3.5 kHz: $morph_{MED}$ = 0.24 ± 0.01 ms vs. $morph_{HIGH}$ = 0.29 ± 0.01, p = 7.7e-10, Fig. 5D). These results were reproduced in the computational model and mirror the patterns observed with gamma-distributed variations (Figs.1 and 3). This suggests that the modulation of GBC output is a robust functional consequence of the morphological heterogeneity of endbulb inputs.

Morphologically plausible input variation impacts encoding of amplitude-modulated sounds

To confirm the impact of realistic input variations on the encoding of amplitude-modulated sounds, we repeated the SAM stimulation experiments using the two morphologically constrained input variations. Consistent with the results from gamma-distributed variations (Fig. 4), the morphologically constrained inputs presented a trade-off between firing rate and temporal precision. Higher input variation elevated overall firing rates (600 Hz: $morph_{MED}$ =

96 ± 38 Hz vs $morph_{HIGH}$ = 125 ± 34 Hz, p = 7.4e-9, n = 19, Fig. 6A), whereas VS and CI were concomitantly reduced (VS at 600 Hz: $morph_{MED}$ = 0.46 ± 0.04 vs $morph_{HIGH}$ = 0.37 ± 0.02, p = 8.1e-12; CI at 600 Hz: $morph_{MED}$ = 1.43 ± 0.07 vs. $morph_{HIGH}$ = 1.26 ± 0.03, p = 1.2e-10, Fig. 6B and C). However, rate-coding fidelity ($Corr_{Norm}$) was enhanced at the 200 Hz modulation frequency under the $morph_{HIGH}$ condition (200 Hz: $morph_{MED}$ = 0.89 ± 0.01 vs $morph_{HIGH}$ = 0.93 ± 0.01 Hz, p = 2.9e-17, Fig. 6D). These findings reinforce the conclusion that the degree of morphological heterogeneity among endbulb inputs critically shapes the balance between temporal and rate-coding strategies during the processing of both simple and complex sounds.

Discussion

The heterogeneity of synaptic inputs converging onto neurons is a fundamental feature of neural circuit design. The strength and variation of these inputs profoundly shape neuronal output, thereby determining a neuron's computational role within its circuit. In this study, we investigated how such input strength variation affects the sound information coding in GBCs which receive multiple, variably sized endbulb inputs from the AN. Our findings demonstrate that the degree of variation among these endbulb inputs critically determines GBC firing characteristics. Specifically, the results reveal a functional trade-off: increased input variation enhances overall firing rates and improves the encoding of stimulus amplitude modulation, yet reduces temporal precision in representing the stimulus fine-structure and increases onset spike jitter. The modeling results, which extend the experimental observations by testing a wider range of input variations, demonstrate that this functional transition occurs continuously. This suggests that morphological variation in synaptic strength enables GBCs to operate along a functional continuum, tuned by their specific input configurations.

Computational mechanisms of synaptic convergence

The computational impact of input variation arises from the interplay of synaptic summation and the GBC's AP threshold. Like other auditory brainstem neurons, GBCs possess low input resistance and a fast membrane time constant, creating a short integration window that is well-suited for temporal processing [63–66]. Notably, our analysis revealed that the observed changes in firing rate and VS were uncorrelated with these intrinsic membrane properties. Instead, GBC output was primarily driven by the degree of input variation, allowing GBCs to operate along a functional continuum.

In the 'no variation' scenario, where all inputs are uniformly subthreshold, AP generation requires the precise temporal summation of multiple synaptic inputs. Consequently, GBCs act as coincidence detectors, filtering out uncorrelated input noise to achieve high temporal precision despite lower firing rates [36,61,67,68]. However, the capacity for input variation to enhance firing rates was frequency-dependent and more prominent during high-frequency

stimulation (Fig. 2B). At low frequencies, the highly synchronized activity of subthreshold inputs generates APs in most stimulation cycles (i.e., high degree of entrainment), effectively placing a ceiling on overall firing rates [36,67,69]. In contrast, the convergence of many desynchronized subthreshold inputs can raise the effective spike threshold, rendering the neuron more selective to highly correlated inputs during sensory encoding [70,71]. The principle of input convergence enhancing temporal precision is not limited to our experimental setting. For instance, experiments using optogenetic stimulation of the AN demonstrated that convergent activation improves temporal precision [72]. Similarly, computational models suggest that the loss of temporal precision in mice with impaired neurotransmitter release can be rescued by increasing synaptic convergence [73]. High input convergence has also been identified as a mechanism to improve temporal fidelity in the visual cortex and in electric fish [74,75].

In contrast, the ‘high variation’ condition, characterized by a mixture of strong and weak inputs, shifts this operational mode by reducing the dependence on input coincidence. If the largest input is suprathreshold (‘high variation’ condition) it can independently drive the cell. Even when all inputs are subthreshold (‘medium variation’), their combined activity depolarizes the membrane and introduces stochastic fluctuations that broaden the integration time window, thereby enhancing the neuron’s responsiveness [27]. This shift in input configuration transforms GBCs into rate encoders, where the output is primarily dictated by the firing rate of the largest input. While a single large input may function similarly to multiple, perfectly synchronized small inputs, the noise-averaging benefits of convergence are lost. As a result, temporal jitter and stochasticity in the strong input translate directly into the GBC output, degrading temporal precision.

The presence of suprathreshold inputs also affects response latency. In theory, strong inputs shorten first-spike latency by triggering an AP without the need for coincidence. Under these conditions, GBCs would act as latency detectors, driven primarily by the input with the earliest arrival time. However, we observed that increased input variation also elevates

spontaneous firing. This elevated baseline activity can obscure the first stimulus-evoked spike, making it difficult to detect statistically against background noise. Indeed, while first spikes may occur earlier in the 'high variation' condition, the minimum first-spike latency calculated as statistical deviation from the spontaneous activity (FSL_{min}) showed slightly longer response latencies. Understanding these underlying mechanisms is critical, as alterations in GBC firing directly shape the input to subsequent stages of auditory processing.

Functional implications for auditory processing

GBCs provide the primary excitatory input to the MNTB, where their large-diameter axons form the calyx of Held synaptic terminals. The calyx–MNTB synapse is a critical relay station [6,63,76–78], providing precisely-timed inhibition to several key nuclei within the superior olivary complex (SOC) involved in sound localization (e.g. medial superior olive, MSO; lateral superior olive, LSO) and temporal gap detection (superior paraolivary nucleus, SPN) [10,79–82].

Our findings, supported by simulations based on detailed EM reconstructions [31], suggest that the GBC population is functionally heterogenous, exhibiting substantial diversity driven by AN input variations. GBCs receiving similarly sized, subthreshold endbulb inputs may function as high-fidelity temporal relays, preserving and even enhancing the temporal precision required for binaural computations on a sub-millisecond timescale for sound localization [31,83–85]. Conversely, GBCs receiving highly variable inputs, characterized by one or two large suprathreshold endbulbs alongside smaller ones, might trade some temporal precision to emphasize a more robust rate code. This enhances their ability to track stimulus envelopes and results in shorter response latencies, but increases temporal jitter. Indeed, morphological data from a limited sample in mice, combined with computational modeling, suggest that roughly half of GBCs operated in a coincidence detection mode, while the other half showed a mixed-mode strategy [31]. Whether this distribution generalizes to

the whole population or differs along the tonotopic axis and across species remains to be investigated.

The implications of GBC heterogeneity on downstream targets are intriguing. Their thick axons project predominantly to the contralateral MNTB, forming the canonical calyx of Held, but some collaterals project to the periolivary nuclei, the VNLL, and the LSO [47,86,87]. The MNTB provides inhibitory inputs to several downstream targets with different functional demands. For instance, the MSO requires precisely timed inputs for interaural time difference (ITD) coding, whereas LSO and SPN may require inputs that are more dependent on sound intensity. The required functional diversity might originate in both the MNTB and its GBC inputs. Indeed, the calyx of Held exhibits considerable structural and functional heterogeneity, irrespective of tonotopic location. For example, MNTB neurons contacted by simple calyces typically show stronger EPSC depression, reflecting differences in release probability [88,89]. Notably, recent work demonstrated that this presynaptic diversity is mirrored by the intrinsic excitability of their postsynaptic target. MNTB neurons receiving simple calyces exhibit lower input resistance, faster membrane time constant and reduced AP fidelity than those contacted by complex calyces [90]. Our current data suggests that input variation alone may be sufficient to shape GBC output, with changes in firing rate and VS being independent of intrinsic membrane properties. However, if presynaptic variation and postsynaptic properties were matched, as seen in the MNTB, this could further amplify the functional diversity among GBCs. It is tempting to speculate that this GBC diversity corresponds to the heterogeneity of their calyx terminals, enabling the MNTB to meet the specific computational demands of its target nuclei. Although direct evidence linking GBC input variation to specific calyx subtypes or SOC targets is currently lacking, a heterogeneous GBC population capable of encoding various stimulus features could diversify MNTB signaling to downstream nuclei.

Biological origin of synaptic variation and methodological considerations

The biological origin of synaptic variation in GBCs remains unclear. One potential source of this heterogeneity is the convergence of different spiral ganglion neuron (SGN) subtypes onto individual GBCs. In mice, for example, BCs receive inputs from multiple SGN subtypes with distinct acoustic response properties [91,92]. In contrast, data from cats suggest that individual BCs are primarily contacted by a single SGN subtype, with type Ia endbulbs being larger than those from type Ic [32,93,94]. If gerbils follow the cat model and SGN subtypes systematically correlate with endbulb size, their interaction during sound stimulation would introduce a heterogeneity not explicitly addressed in the current approach. In mice, however, SGN inputs onto the same BC exhibit comparable short-term plasticity [91,95,96], and BCs with varying SGN proportions display similar firing thresholds and spontaneous rates [91]. This suggests that intrinsic variations in synapse size, potentially independent of SGN subtype, are the primary drivers of the observed functional effects.

Beyond SGN subtype identity, heterogeneity in frequency tuning and developmental plasticity may also contribute to input variation. Physiological studies in cats indicate that some GBCs may integrate inputs from AN fibers tuned to slightly different frequencies [97,98]. If large and small inputs were tuned differently, this would profoundly affect their functional convergence during complex acoustic stimuli, such as frequency sweeps. Furthermore, it is unknown whether this variation reflects a random outcome of synapse elimination during development or a dynamic feature shaped by auditory experience. In both rodents and cats, endbulb size changes with sound exposure, demonstrating the potential for activity-dependent modulation [99–103]. Such plasticity could provide a mechanism for neuronal adaptation without requiring synapse elimination. These unresolved biological factors present specific limitations for our study. Our recordings were performed in Mongolian gerbils, a species for which detailed anatomical data on input convergence is currently lacking. Nevertheless, the consistent effect of input variation across GBCs suggests that the underlying mechanism is robust and largely independent of the exact number of endbulbs terminating on a single neuron. The ability of the model to replicate these effects further

implies that this mechanism functions across species-specific differences in input number and variation. By constraining input variations to morphological data from mouse GBCs [31], we demonstrated that biologically plausible variations in input size are sufficient to induce the observed effects on GBC coding.

Our experimental and modeling approaches assumed a linear summation of statistically independent synaptic inputs. This assumption was chosen based on the observation that endbulb terminals are generally distributed across the GBC's somatic surface, likely minimizing interactions between them [31,38]. While this model captured the core phenomena and revealed a consistent effect across individual neurons, biological GBCs likely exhibit additional complexities, particularly *in vivo*. For example, multiple endbulbs originating from the same AN fiber or exhibiting highly correlated activity could function as a single, large input, thereby reducing the effective degree of variation. Additionally, morphological evidence suggests that larger inputs often terminate near the axon initial segment, potentially amplifying their synaptic efficacy beyond size alone [31]. Finally, while GBC dendrites are typically short, they may receive additional synaptic inputs that could modulate integration dynamics and excitability in a state-dependent manner [31,33,34,62,104,105]. Despite these simplifications, the consistent reproduction of key experimental findings in the computational model supports the conclusion that input variation is a key regulator of GBC output. Future studies employing large-scale electron microscopy reconstructions across multiple ages and CN locations could provide the necessary structural details to investigate how these effects are impacted by modulatory influence such as somatic and dendritic inhibition [106–113].

Input heterogeneity as a general coding strategy

The integration of strong and weak synaptic inputs is a fundamental principle of neural circuit design, evident in the spinal cord and various brain regions, including the cortex and thalamus [22–26,114,115]. This organization allows neurons to perform complex computations and is found across multiple sensory systems, often beginning at the

periphery. Synapses between the inner hair cells and the contacting SGN exhibit different calcium sensitivities and release probabilities. This arrangement creates parallel output channels from the same inner hair cell, each with distinct sensitivities and thresholds [116]. Similarly, in the cerebellum, granule cells are innervated by mossy fibers with varying strengths and short-term plasticity profiles, a heterogeneity thought to enable pathway-specific responses that improve temporal coding of multisensory inputs [117]. Cerebellar nuclei receive inhibitory inputs of highly variable sizes from Purkinje cells, allowing them to convey both rate codes and precise temporal information [28]. A similar principle of variable input strength is found in barrel cortex [27]. In each of these cases, similar to GBCs, structural heterogeneity expands the encoding capacity of the neural circuit.

At the network level, neuronal heterogeneity is considered essential for maximizing computational power. Theoretical and experimental work in the cortex has shown that diversity in both synaptic weights and intrinsic cellular properties is critical for robust stimulus encoding and learning [118–120]. Heterogeneous neuronal populations are more effective in learning tasks with complex temporal structures [121] and provide a richer, more reliable representation of sensory information [4,122].

Our findings place GBCs within this broader framework by illustrating how synaptic input variation can generate diverse output streams, some optimized for temporal fidelity and others optimized for rate. This heterogeneity might therefore be critical for tailoring information coding to the different computational demands of downstream auditory circuits.

Methods

Ethics statement

All experiments were conducted at the Physiology Laboratories of the Department for Human Medicine at the University of Oldenburg. Experimental protocols were approved by the University's Animal Welfare Office and carried out in accordance with the German Animal

Welfare Act (§4 TSchG) and European Union Directive 2010/63/EU (protocol number: Milenkovic TschG 4 (3)). Every effort was made to minimize the number of animals used and to alleviate potential pain or distress.

Animals

Mongolian gerbils (*Meriones unguiculatus*) were bred at the central animal facility of the University of Oldenburg. Animals were group-housed under a standard 12-h light/dark cycle with *ad libitum* access to food and water. Experiments were performed on young adults (postnatal day P20–P25) of both sexes (n = 35; 12 female).

Method details

Acute brain slice preparation

Following rapid decapitation, acute parasagittal slices (200 µm thickness) containing the CN were prepared using a vibrating microtome (Leica VT1200 S) equipped with zirconia ceramic blades (EF-INZ10, Cadence Blades). Slicing was performed in ice-cold, low-calcium artificial cerebrospinal fluid (aCSF) containing (in mM): 125 NaCl, 2.5 KCl, 0.1 $CaCl_2$, 3 $MgCl_2$, 1.25 NaH_2PO4, 25 $NaHCO_3$, 10 glucose, 3 myo-inositol, 2 sodium pyruvate, and 0.4 ascorbic acid. The aCSF was continuously oxygenated with carbogen (5% CO_2 and 95% O_2) and maintained at pH 7.4. Slices were then transferred to a holding chamber containing standard recording solution at near-physiological temperature (36–37°C; identical to the slicing aCSF, except $CaCl_2$ and $MgCl_2$ were adjusted to 1.2 mM and 1 mM, respectively), allowed to recover for 30–45 min, and stored thereafter until recording. All solutions were prepared using ultrapure water (0.055 µS/cm).

Electrophysiology

Slices were placed in a recording chamber continuously perfused with oxygenated aCSF (~1 mL/min) and maintained at ~37°C using a dual automatic temperature controller (TC-344B, Warner Instruments). Neurons were visualized using an upright microscope (Axioskop

2 FS plus, Zeiss) with a water-immersion 63x objective (W Plan-Apochromat 63x/1.0, Cat# 421480-9900-000, Zeiss) and a CCD camera (IR-1000, DAGE-MTI).

Recording pipettes were pulled from borosilicate glass (GB-150F-8P, Science Products) to a resistance of 3–5 MΩ when filled with intracellular solution containing (in mM): 120 K-gluconate, 20 KCl, 5 EGTA, 10 HEPES, 0.05 $CaCl_2$, 5 Na_2-phosphocreatine, 4 Mg-ATP, and 0.3 Na-GTP, supplemented with 0.2% biocytin for post-hoc morphological verification. Voltages were corrected for a calculated liquid-junction potential of 12 mV. Whole-cell recordings were made using a Multiclamp 700B amplifier (Molecular Devices), digitized at a 100 kHz sampling (Digidata 1440A interface, Molecular Devices) and acquired using pClamp software (RRID:SCR_011323, version 11.2.2, Molecular Devices). In current-clamp mode, resting membrane potential was held near -72 mV using a small bias current (<140 pA). Series resistance (<10 MΩ) was fully compensated via bridge balance. Pipette capacitance neutralization and bridge balance were monitored and adjusted throughout. Intrinsic membrane properties were characterized for a subset of GBCs (70/83, 84%) using a 200 ms square current pulse (50-100 pA).

Simulating auditory nerve fiber input

Spiking activity of AN fibers was simulated using the 2018 version of the auditory periphery model [40] in the ‘cat’ configuration, as gerbil AN fiber responses resemble those of cats [123–125]. Since GBCs primarily receive inputs from high-spontaneous rate (SR) type Ia SGN [32,91,92], model fiber SR was set to 70 spikes/s. Refractory periods were fixed at the midpoint of the model’s default parameter range, representing typical physiological values (absolute: 0.45 ms, relative: 0.5125 ms).

Consistent with anatomical evidence that GBCs receive around 5 to 12 endbulb inputs in mice and around 20 in cats [31,34], we simulated the convergence of 10 AN inputs per GBC. Given the narrow frequency tuning of GBCs [69], all converging simulated AN fibers shared the same characteristic frequency (CF). For pure-tone stimuli, the fibers' CF matched the tone frequency; for amplitude-modulated (AM) sounds, the CF matched the carrier

frequency. Sound intensity was 70 dB SPL for pure tones and 25 dB SPL for AM sounds. Tone stimuli were simulated for 200-500 ms with an identical pause between repetitions to mimic stimulation paradigms used during *in vivo* recordings [107,126–128]. The AN spike pattern for a given stimulus remained fixed across cells and variation conditions.

Controlling synaptic input variation

To investigate the impact of input heterogeneity, we systematically varied the strength of the 10 simulated AN fibers. Synaptic input variation (*v)* was quantified as the coefficient of variation, defined as the standard deviation (*s)* of the 10 AN input amplitudes divided by their mean (m; i.e., v = s/m). We used a gamma distribution (shape parameter $a = 1/v^2$, scale parameter $b = mv^2$) to create three conditions: 'no variation' (v = 0), 'medium variation' (v = 0.4), and 'high variation' (v = 1) (Fig. 1B). These levels cover a broad range of synaptic size heterogeneity, including the range reported from anatomical estimates of GBC inputs [31].

To isolate the effect of input variation, average input strength was first adjusted to 7-14 nS to elicit GBC firing rates of >100 spikes/s during 350 Hz stimulation. This average input strength was held constant across conditions. In the 'no variation' condition, all inputs had equal strength and were functionally subthreshold. The 'medium variation' condition featured inputs ranging from 3-6 nS (smallest input) to 12.5-25 nS (largest input) with all inputs remaining subthreshold. In the 'high variation' condition, inputs ranged from 0.2-0.4 nS (smallest) to 23-46 nS (largest), with one suprathreshold input. Total charge between conditions was nearly identical (<2% difference), reflecting the stochasticity of AN fiber discharges. Stimuli were presented sequentially while monitoring cell vitality to exclude time-dependent confounds.

To confirm the biological relevance of our findings, we also implemented synaptic strength distributions based on the morphological data [31]. Two representative GBC input data sets were selected: one (GBC21) previously characterized as fitting the coincidence detection model (CV ≈ 0.33, approximating our 'medium variation', $morph_{MED}$) and another (GBC18L)

fitting the mixed-mode integration model (CV ≈ 0.8, approximating our 'high variation', $morph_{HIGH}$). To facilitate comparison between these two morphologically derived input variations, we used eight AN inputs for both conditions.

Conductance-clamp implementation

Synaptic conductance traces (G_{syn}) were generated by convolving simulated AN spike trains with a stereotypical EPSC waveform, modeled as alpha-function with a time constant of 0.2 ms. EPSC amplitudes were scaled according to the input variation condition. Total G_{syn} was calculated as the linear sum of conductances from all AN fibers.

Conductance-clamp was implemented as described previously [129]. Briefly, the instantaneous GBC membrane potential (V_m) was digitized (PCIe-6361 via BNC-2120 interface, National Instruments) and fed into a separate computer running mafDC (courtesy of M. A. Xu-Friedman) in Igor Pro (RRID:SCR_000325, version 8, Wavemetrics). The appropriate AMPA current (I_{syn}) was calculated in real-time (latency: 15 µs, AMPAR cycle time: 8 µs), according to Ohm's law, assuming a reversal potential (E_{syn}) of -12 mV, and injected back into the GBC via the recording electrode:

$$I_{syn} = G_{syn}\,(V_m - E_{syn}).$$

Post-hoc morphological identification of GBCs

To morphologically confirm GBC identity, slices with biocytin-filled neurons were fixed with 4% paraformaldehyde (PFA) in 1x phosphate-buffered saline (PBS) overnight at 4°C. Following fixation, slices were rinsed in 1x PBS (6 × 5 min) and 1x PBS with 0.3% TritonX-100 (PBST, 6 × 5 min). To visualize biocytin-filled GBCs, slices were incubated for 2.5 h at room temperature with Cy5-conjugated streptavidin (5 µg/mL in PBST, Cat#016-170-084, Jackson ImmunoResearch). After final rinses with PBST (6 × 5 min), PBS (2 × 5 min) and ultrapure water (2x5 min) slices were mounted on glass slides (Aqua-Poly/Mount, Cat#18606, Polysciences, Inc.). Confocal images were acquired on a Leica SP8 confocal scanning microscope equipped with a 10x (0.3 NA, Cat#11506505) dry objective and a 63x (1.4 NA, Cat#11506350) oil-immersion objective using a 647 nm excitation wavelength.

Globular bushy cell model

Computational simulations of GBC responses were performed using a modified version of the "adaptive coincidence-counting model" [4]. Each simulated AN spike evoked a simplified rectangular postsynaptic response (Fig. 2A) of constant duration (W) but variable amplitude (A) depending on the variation condition. These responses were linearly summed to produce the total integrated input u(t). The model generated an output spike when u(t) exceeded an adaptive threshold θ(t), followed by an absolute refractory period (R) during which no further spikes could be triggered.

The adaptive threshold consisted of static and dynamic components: $\theta(t) = \theta_S + \theta_D(t)$. The static component θ_S was fixed at 1, so that postsynaptic response amplitudes (A) were considered normalized to this static input threshold. The dynamic component θ_D changed according to the total input amplitude: $T(d\theta_D/dt) = -\theta_D(t) + S \cdot (u(t))^2$, where T is the time constant and S is the strength of adaptation [4]. The quadratic exponent of u(t) was designed to approximate the nonlinear activation of various adaptive mechanisms in BC, such as low-threshold K^+ channels and inhibitory feedback from other CN neurons. This adaptive threshold mechanism allowed the model to reject poorly synchronized inputs (Fig. 2A). The spike generation mechanism implemented in the GBC model is deterministic and does not produce spike time jitter. To simulate this intrinsic variability, a spike-generation delay $D_{spike} = D_{fix} + D_{rand}$ was added to each output spike timing. The fixed component D_{fix} was set to 0.2 ms, and the random component D_{rand} was drawn from an alpha distribution with a time constant of 0.1 ms [130]. This modification was based on the spike latency data from pure-tone stimulation (Fig. 3B5 and 3B6) and increased response latency by 0.4 ms (SD = 0.14 ms).

Model parameters and validation

The GBC model included five free parameters (Table 1). A default set was established to match experimental pure-tone responses (e.g., PSTHs and raster plots in Fig. 3). To confirm the robustness of the modeling results, we systematically varied parameters around this

default (Table 1, right column). Each "model instance", representing a unique parameter combination, was tested with pure-tone stimulation. Only those instances exhibiting GBC-like responses, as defined by the quantitative criteria described below, were adopted for further simulations.

The adoption criteria were based on our experimental observations (Figs. 1 and 3). Model instances were required to satisfy the following criteria: (1) spontaneous rate of 10–60 spikes/s; (2) for 350 Hz stimulation: steady-state driven rate >180 spikes/s and vector strength >0.85; (3) for 3500 Hz stimulation: steady-state driven rate of 80–180 spikes/s and onset spike probability >0.95. Furthermore, the PSTH shape near the onset of the 3500 Hz tone was examined to ensure a primary-like-with-notch (PL_N) spiking pattern, characterized by a sharp peak followed by a notch (pause of spiking activity) and a smooth recovery towards the steady-state spiking response (Fig. 3A2). Specific criteria for the PL_N response were: (4) the notch appeared within 3 ms after the onset peak; (5) the notch amplitude (minimum rate in PSTH) was below 50% of the steady-state spike rate; (6) a second peak in the PSTH was absent or below 300 spikes/s; (7) the average spike rate at 6–10 ms after the stimulus onset was >90% of the steady-state spike rate; and (8) a second notch was absent or higher than 50% of the steady-state spike rate. The last criterion was used to distinguish PL_N-type PSTHs from chopper-type PSTHs [4]. Of the 28,812 model instances tested, 313 (1.1%) met all of these physiological response criteria to be considered ‘GBC’ and were used for simulations.

Quantification and statistical analysis

Individual GBCs were treated as independent biological samples. Aggregated data are presented as mean ± standard deviation, unless otherwise noted. All comparisons involved within-cell manipulations (i.e., stimulus type and input variation for the same cell) and were analyzed using a multifactorial repeated-measures ANOVA (two-way RM ANOVA). Post-hoc multiple comparisons were corrected using the Bonferroni method [131]. A p-value <0.05 was deemed statistically significant for all interpretations. As no sex difference was found for

firing rate ($p = 0.25$) or temporal precision ($p = 0.86$), data were pooled for further analysis. Sample sizes were determined based on variance observed in similar studies. No statistical methods were used to pre-determine sample sizes prior to data collection.

Electrophysiological data analysis

Data analysis was performed using custom-written scripts in MATLAB (RRID:SCR_001622, Version 2024b, The Mathworks). Input resistance was derived from a linear fit to the current-voltage relationship in response to a square current pulse, while the membrane time constant was estimated by fitting a single-exponential function to the initial phase of the voltage deflection. Action potentials (APs) were detected at -20 mV threshold, and all detected spikes were visually inspected and curated to exclude potential artifacts. For all subsequent analyses, the time of the AP peak was used as the spike time. Average firing rates were calculated for evoked (200–500 ms duration) and spontaneous (150 ms duration) epochs. Correlations were assessed using Spearman's rank [132]. Onset probability was calculated as the fraction of trials with at least one AP within 1.5 ms of the response onset. Minimum first-spike latency (FSL_{min}) was defined as the time between stimulus onset and the detection of a statistically significant firing rate increase ($p < 1e\text{-}6$) above the spontaneous rate [49]. This method avoids the ambiguity in identifying the first stimulus-evoked spike caused by varying spontaneous firing rates. First-spike jitter was quantified as the standard deviation of spike latencies occurring within a window from 0.6 ms before and 1.2 ms after FSL_{min}. Peristimulus time histograms (PSTH) were constructed using 0.5 ms bin width across 100–200 repetitions. Phase-locking to periodic stimuli (pure tones or SAM) was quantified by vector strength (VS) [41]. Spike timing precision was assessed by correlation index (CI), and calculated as the normalized peak height of the shuffled autocorrelogram, constructed across repeated presentations of identical stimuli [58,59]. Envelope tracking for SAM stimuli was quantified by cross-correlation ($Corr_{Norm}$) between the stimulus envelope and the corresponding response PSTH, after correcting for the neuron's response latency [106,133]. Note that $Corr_{Norm}$ values range from 0 to 1; unmodulated responses typically yield a $Corr_{Norm}$

value around 0.82, while values >0.9 indicate robust tracking of the stimulus envelope. Entrainment index (EI) was used to quantify the proportion of interspike intervals within 0.5 – 1.5 times the stimulus period [36].

Resource Availability

Lead contact

Requests for further information and resources should be directed and will be fulfilled by Ivan Milenkovic (ivan.milenkovic@uol.de) or Go Ashida (go.ashida@uol.de).

Data and code availability

All numerical data and model code used to generate figures are available at https://doi.org/10.17632/2tbkzdpjy6 under the terms of Creative Commons Attribution 4.0 License (CC BY 4.0).

Acknowledgments

This work was funded by the Deutsche Forschungsgemeinschaft (DFG, German Research Foundation) under Germany's Excellence Strategy – EXC 2177/1 - Project ID 390895286 to GA, the Open Access Publication Funding (DFG) and intramural funding to CK (Carl von Ossietzky Universität Oldenburg; FP 2024-099). The authors acknowledge the Fluorescence Microscopy Service Unit, Carl von Ossietzky University of Oldenburg, for the use of the imaging facilities.

Author contributions:

CW: Investigation; **GA:** Conceptualization, Methodology, Software, Verification, Formal Analysis, Resources, Data Curation, Writing – Review & Editing; **CK:** Conceptualization, Methodology, Software, Verification, Formal Analysis, Resources, Data Curation, Writing –

Original Draft, Writing – Review & Editing, Visualization, Supervision, Funding acquisition; **IM:** Conceptualization, Resources, Writing – Review & Editing, Supervision, Project administration

Declaration of interests

The authors declare no competing interests

Figure Legends

Fig. 1: Synaptic input variation increases firing rates at the expense of temporal precision. **(A)** GBC identification based on morphological and electrophysiological features. **(A1)** Left: Low-magnification image of cochlear nucleus parasagittal slice containing a biocytin-filled GBC near the AN root (arrow). AVCN: anteroventral cochlear nucleus; PVCN: posteroventral cochlear nucleus; DCN: dorsal cochlear nucleus; AN: auditory nerve. Right: High-magnification image of the same GBC, displaying its characteristic round soma and short dendrites. **(A2)** Left: Electrophysiological signature of a GBC (top) responding with one or a few APs at the onset of suprathreshold depolarizing current (bottom) and voltage sag in response to hyperpolarizing current injection. Right: Population data (n = 70) of GBC input resistance and membrane time constant. **(B)** Schematic of the experimental paradigm: Acoustic stimuli (top) were processed by an auditory nerve model to generate spike trains for 10 AN fibers (ANF1-10). These spike trains were convolved with the EPSC waveform to generate conductance templates with varying synaptic strengths, ranging from ‘no variation’ (blue) to ‘high variation’ (orange), and injected into GBCs. Histograms illustrate the input distributions for the conditions used. The GBC response (bottom right) was recorded, and AP number and timing (gray triangles) were analyzed. **(C1)** Population data (n = 15) of the average GBC firing rate in response to pure-tone stimuli (350, 1000, and 3500 Hz) under three input conditions (blue: ‘no variation’, green: ‘medium variation’, orange: ‘high variation’). Gray triangles: AN input. Firing rates increased with input variation for 1000 Hz and 3500 Hz stimulation. **(C2)** Vector strength, as a measure of temporal precision, decreased with input variation, particularly at lower frequencies. Boxplots show median and interquartile range (IQR, whiskers: 1.5 × IQR). Individual cells are represented by gray circles. P-values: 2-way

RM ANOVA with Bonferroni post-hoc tests (n = 15). The data underlying this Figure are available at https://doi.org/10.17632/2tbkzdpjy6.

Fig. 2: Adaptive coincidence-counting model reproduces experimental data across a wide range of input variations (A) Schematic of GBC model. Top: Example spike trains of four AN fibers highlighting different spike synchrony. Middle: Model responses to AN fiber inputs with no (blue) and high (orange) input variations. The adaptive threshold changes dynamically according to the recent history of summed inputs (internal state). GBC model output spikes are generated when the summed inputs exceed this threshold (blue and orange circles). Note that in the 'high variation' condition, strong individual inputs can generate GBC spikes with little dependence on coincidence **(B)** Average firing rates for 313 GBC model instances in response to pure-tone stimuli (350, 1000, and 3500 Hz). Colored data indicate input variations used in the *in vitro* experiments (blue: 'no variation'; green: 'medium variation'; orange: 'high variation'). The model reproduces the experimental trend of higher firing rates for larger input variations at high frequencies. **(C)** Vector strength reduced with increasing input variation, mirroring the experimental results. Box plots show the range of values from all 313 model instances with thick, medium, and thin boxes indicating 25–75, 10–90, and 0–100 percentiles, respectively. The data underlying this Figure are available at https://doi.org/10.17632/2tbkzdpjy6.

Fig. 3: Synaptic input variation increases sustained firing rates but reduces onset spike-time precision. **(A1)** Peristimulus time histogram (PSTH) of the average AN input responding to a 3500 Hz pure-tone. Note the sharp onset followed by adaptation to a sustained rate. **(A2)** Representative GBC output PSTH for the input in A1 under 'no variation' (blue) and 'high variation' (orange). **(A3)** Output of the GBC model in response to the same conditions, mirroring experimental data. Insets in A2-A3 show a magnified view of the response onset, highlighting the reduced onset peak under the 'high variation' condition. **(B)** Experimental population data (n=17) for different input variations (blue: 'no variation', green: 'medium variation', orange: 'high variation'). **(B1)** Raster plot (15 repetitions) of the first spike

within 1.5 ms of stimulus onset during ‘no variation’ (top, blue) and ‘high variation’ (bottom, orange) conditions. Note the slightly earlier but more variable first spike in the ‘high variation’ condition. **(B2)** Onset spike probability was significantly reduced with input variation. **(B3–B4)** sustained firing rates (50-200 ms) and spontaneous firing rates increased with input variation. Gray triangles: mean AN input. **(B5–B6**) Minimum first-spike latency decreased, while first-spike jitter increased with input variation. **(C1-C6)** Output of the GBC model quantifying the same parameters as for the experimental data in B1-B6. Colored box plots indicate the input variations used in the *in vitro* experiments. In B) box plots show median, IQR (whiskers: 1.5 × IQR) with individual cells shown as gray circles. In C) box plots for modeling data show the range of values from all 313 model instances with percentiles (thick: 25–75, medium: 10–90, thin: 0–100). P-values: 2-way RM ANOVA with Bonferroni post-hoc tests (n = 17). The data underlying this Figure are available at https://doi.org/10.17632/2tbkzdpjy6.

Fig. 4: Synaptic input variation shapes GBC encoding of amplitude-modulated sounds. **(A1)** Simulated AN fiber response to a 200 Hz amplitude-modulated sound (top). The AN firing rate was robustly modulated by the stimulus envelope. Note that the stimulus was aligned with the AN firing rate modulation for display purposes. **(A2)** PSTHs of a representative GBC responding to input in A1. Note the broader peaks in the 'high variation' (orange) condition compared to 'no variation' (blue). **(A3)** GBC model response to the same input, reproducing the general PSTH shape, including broader peaks in the 'high variation' condition. **(B)** Population data (n=15) for modulation frequencies of 200, 600, and 2000 Hz. Left: Experimental data; Right: Model responses. Gray triangles: mean AN input **(B1)** Average firing rates generally increased with input variation. **(B2–B3)** Vector strength and correlation index decreased significantly with input variation. **(B4–B5)** Entrainment index and normalized cross-correlation ($Corr_{Norm}$) increased with input variation at low modulation frequencies but remained unchanged at high frequencies. Box plots containing experimental data show median and IQR (whiskers: 1.5 × IQR). Individual cells shown as gray circles. Box plots for modeling data show the range of values from all 313 model instances with percentiles (thick: 25–75, medium: 10–90, thin: 0–100). P-values: 2-way RM ANOVA with Bonferroni post-hoc tests (n = 15). The data underlying this Figure are available at https://doi.org/10.17632/2tbkzdpjy6.

Fig. 5: **Morphological input variation drives GBC functional heterogeneity**. Population data (n = 17) comparing responses to pure-tone stimulation under two input variation conditions derived from morphological estimates: 'medium variation' (CV ≈ 0.33, green, GBC21) and 'high variation' (CV ≈ 0.8, orange, GBC18L) [31]. Histogram illustrates the strength distribution of eight AN inputs used. **(A)** Left: High input variation enhanced GBC firing at 1000 and 3500 Hz, with no effect at 350 Hz. Right: GBC model responses corroborated the experimental results. **(B)** Temporal precision was reduced when GBCs received highly variable inputs. **(C–D)** Minimum first-spike latency was slightly longer at the 'high variation' condition (C) and accompanied by an increase in first-spike jitter (D). Box plots containing experimental data show median and IQR (whiskers: 1.5 × IQR). Individual cells are shown as gray circles. Box plots for modeling data show the range of values from all 313 model instances with percentiles (thick: 25–75, medium: 10–90, thin: 0–100). P-values: 2-way RM ANOVA with Bonferroni post-hoc tests (n = 17). The data underlying this Figure are available at https://doi.org/10.17632/2tbkzdpjy6.

Fig. 6: Morphologically constrained input variation differentially affects temporal precision and envelope encoding of amplitude-modulated sounds. Population data (n = 19) comparing GBC responses to SAM stimuli under two morphologically constrained input variations: 'medium variation' (CV ≈ 0.33, green, GBC21) and 'high variation' (CV ≈ 0.8, orange, GBC18L) [31]. **(A)** High input variation enhanced firing rates. **(B-C)** High input variation decreased vector strength (B) and correlation index (C). **(D)** High input variation improved representation of the stimulus envelope ($Corr_{Norm}$). All results were successfully reproduced in the computational model. Box plots containing experimental data show median and IQR (whiskers: 1.5 × IQR). Individual cells are shown as gray circles. Box plots for modeling data show the range of values from all 313 model instances with percentiles (thick: 25–75, medium: 10–90, thin: 0–100). P-values: 2-way RM ANOVA with Bonferroni post-hoc tests (n = 19). The data underlying this Figure are available at https://doi.org/10.17632/2tbkzdpjy6.

Tables

Table 1: Model parameters. The total number of parameter combinations was 12×7×7×7×7 = 28,812. The default parameter values were used for Figs. 3A3, 3C1, 4A3.

Parameter	Default value	Ranges tested
(mean) Input amplitude *A*	0.38	0.28 − 0.50 (step 0.02)
Input duration (ms) *W*	0.6	0.2 − 1.4 (step 0.2)
Refractory period (ms) *R*	1.5	0.8 − 2.0 (step 0.2)
Adaptation strength *S*	0.8	0.4 − 1.6 (step 0.2)
Adaptation time constant (ms) *T*	0.7	0.3 − 2.1 (step 0.3)

Table 2: Summary of statistical analysis for gamma-distributed input variations

			Variation				
		Stimulus	**no**	**medium**	**high**	**p-value RM ANOVA**	**post-hoc comparisons**
Figure 1 (n=15)	**Firing Rate (Hz)**	**350** Hz	251 ± 53	245 ± 53	234 ± 40	variation: p=4.6e-5	no vs medium: p=0.1 no vs high: p=0.01 medium vs. high: p=0.05
		1000 Hz	135 ± 49	143 ± 47	175 ± 35		no vs medium: p=0.03 no vs high: p=7.9e-6 medium vs. high: p=6.6e-6
		3500 Hz	122 ± 48	134 ± 49	174 ± 34		no vs medium: p=5.5e-5 no vs high: p=8.9e-7 medium vs. high: p=1.4e-5
	Vector Strength	**350** Hz	0.86 ± 0.02	0.85 ± 0.01	0.81 ± 0.01	variation: p=3.7e-6	no vs medium: p=0.001 no vs high: p=3.3e-8 medium vs. high: p=4.3e-8
		1000 Hz	0.61 ± 0.08	0.59 ± 0.09	0.57 ± 0.06		no vs medium: p=0.43 no vs high: p=0.005 medium vs. high: p=0.29
		3500 Hz	0.06 ± 0.03	0.05 ± 0.03	0.05 ± 0.02		no vs medium: p=0.57 no vs high: p>0.99 medium vs. high: p>0.99
Figure 3 (n=15)	**Onset probability**	**3500** Hz	0.97 ± 0.02	0.96 ± 0.02	0.94 ± 0.02	p=3.5e-6	no vs medium: p=0.42 no vs high: p=7.3e-5 medium vs. high: p=4e-4
	Sustained firing rate (Hz)	**3500** Hz	71.7 ± 26.8	86.6 ± 29.7	130.8 ± 28.2	p=8.7e-16	no vs medium: p=5.8e-5 no vs high: p=3.2e-11 medium vs. high: p=2.7e-12
	Spontaneous firing rate (Hz)	**3500** Hz	24.8 ± 14.3	34.8 ± 17.8	65 ± 14.7	p=2.4e-17	no vs medium: p=9e-4 no vs high: p=4.9e-11 medium vs. high: p=1.8e-9
	Minimum first-spike latency (ms)	**3500** Hz	2.83 ± 0.11	2.82 ± 0.1	2.88 ± 0.09	p=8.8e-8	no vs medium: p=0.05 no vs high: p=4.5e-4 medium vs. high: p=1.7e-7
	First-spike jitter (ms)	**3500** Hz	0.22 ± 0.02	0.24 ± 0.02	0.27 ± 0.02	p=7.3e-13	no vs medium: p=8e-4 no vs high: p=1.6e-9 medium vs. high: p=5e-6
Figure 4 (n=15)	**Firing Rate (Hz)**	**200** Hz	130 ± 36	131 ± 33	145 ± 23	variation: p=3e-10	no vs medium: p>0.99 no vs high: p=0.01 medium vs. high: p=0.002
		600 Hz	67 ± 50	77 ± 50	115 ± 38		no vs medium: p=3e-4 no vs high: p=1.47e-7 medium vs. high: p=3.5e-6
		2000 Hz	65 ± 50	71 ± 46	111 ± 43		no vs medium: p=0.12 no vs high: p=7.8e-9 medium vs. high: p=1.4e-9
	Vector Strength	**200** Hz	0.84 ± 0.03	0.83 ± 0.02	0.76 ± 0.01	variation: p=5.7e-14	no vs medium: p=0.006 no vs high: p=9.3e-10 medium vs. high: p=1.6e-12
		600 Hz	0.51 ± 0.06	0.48 ± 0.05	0.37 ± 0.03		no vs medium: p=2.2e-6 no vs high: p=7.2e-10 medium vs. high: p=9.6e-10
		2000 Hz	0.01 ± 0.01	0.01 ± 0.01	0.01 ± 0		no vs medium: p=0.84 no vs high: p>0.99 medium vs. high: p=0.1
	Correlation Index	**200** Hz	3.06 ± 0.19	2.93 ± 0.1	2.39 ± 0.06	variation: p=5.9e-13	no vs medium: p=4e-4 no vs high: p=3.7e-10 medium vs. high: p=1.3e-12
		600 Hz	1.53 ± 0.12	1.46 ± 0.1	1.26 ± 0.04		no vs medium: p=6.2e-6 no vs high: p=3e-8 medium vs. high: p=2.6e-8

		2000 Hz	1.01 ± 0.02	1.01 ± 0.02	1 ± 0.01		no vs medium: p>0.99 no vs high: p=0.5 medium vs. high: p=0.06
	Entrainment Index	**200** Hz	0.6 ± 0.17	0.62 ± 0.17	0.68 ± 0.1	variation: p=4.7e-6	no vs medium: p=0.87 no vs high: p=0.01 medium vs. high: p=0.04
		600 Hz	0.01 ± 0.01	0.01 ± 0.03	0.04 ± 0.05		no vs medium: p=0.36 no vs high: p=0.005 medium vs. high: p=0.001
		2000 Hz	0 ± 0	0 ± 0	0 ± 0		no vs medium: p=0.44 no vs high: p=0.64 medium vs. high: p>0.99
	$Corr_{Norm}$ ¶	**200** Hz	0.87 ± 0.02	0.88 ± 0.01	0.93 ± 0.01	variation: p=1.8e-10	no vs medium: p=0.004 no vs high: p=2.5e-10 medium vs. high: p=6.3e-11
		600 Hz	0.99 ± 0.01	0.99 ± 0	0.98 ± 0.01		no vs medium: p=0.027 no vs high: p=0.5 medium vs. high: p=0.003
		2000 Hz	0.82 ± 0.01	0.82 ± 0.01	0.82 ± 0		no vs medium: p>0.99 no vs high: p=0.42 medium vs. high: p=0.26

Table 3: Summary of statistical analysis for morphologically-derived input variations

		Stimulus	**$morph_{MED}$**	**$morph_{HIGH}$**		**post-hoc comparison ($morph_{MED}$ vs $morph_{HIGH}$)**
Figure 5 (n=17)	**Firing Rate (Hz)**	**350** Hz	154 ± 37	161 ± 30	p=3.7e-11	p=0.05
		1000 Hz	94 ± 28	121 ± 33		p=3.8e-9
		3500 Hz	88 ± 22	120 ± 26		p=1.3e-10
	Vector Strength	**350** Hz	0.86 ± 0.01	0.82 ± 0.01	p=2.6e-8	p=2e-10
		1000 Hz	0.65 ± 0.04	0.62 ± 0.05		p=5.3e-5
		3500 Hz	0.02 ± 0.01	0.02 ± 0.01		p=0.41
	Minimum first-spike latency (ms)	**350** Hz	4.54 ± 0.09	4.61 ± 0.1	p=2.2e-7	p=2e-4
		1000 Hz	4.14 ± 0.05	4.16 ± 0.07		p=0.01
		3500 Hz	2.84 ± 0.07	2.91 ± 0.07		p=5.3e-7
	First-spike jitter (ms)	**350** Hz	0.24 ± 0.01	0.29 ± 0.02	p=3.4e-7	p=2.5e-10
		1000 Hz	0.18 ± 0.05	0.24 ± 0.04		p=0.002
		3500 Hz	0.24 ± 0.01	0.29 ± 0.01		P=7.7e-10
Figure 6 (n=19)	**Firing Rate (Hz)**	**200** Hz	134 ± 30	142 ± 27	p=2.9e-10	p=2e-5
		600 Hz	96 ± 38	125 ± 34		p=7.4e-9
		2000 Hz	89 ± 36	125 ± 31		p=6.2e-11
	Vector Strength	**200** Hz	0.81 ± 0.02	0.75 ± 0.02	p=3.8e-15	p=2e-17
		600 Hz	0.46 ± 0.04	0.37 ± 0.02		p=8.1e-12
		2000 Hz	0.01 ± 0.01	0.01 ± 0		p=0.07
	Correlation index	**200** Hz	2.78 ± 0.11	2.33 ± 0.1	p=2.5e-18	p=3.7e-19
		600 Hz	1.43 ± 0.07	1.26 ± 0.03		p=1.2e-10
		2000 Hz	1 ± 0.01	1 ± 0		p=0.19
	$Corr_{Norm}$	**200** Hz	0.89 ± 0.01	0.93 ± 0.01	p=3.8e-11	p=2.9e-17
		600 Hz	0.99 ± 0.01	0.98 ± 0		p=0.002
		2000 Hz	0.81 ± 0.01	0.82 ± 0.01		p=0.04

References

1. Blackburn CC, Sachs MB. Classification of unit types in the anteroventral cochlear nucleus: PST histograms and regularity analysis. J Neurophysiol. 1989;62: 1303–1329.

2. Doucet JR, Ryugo DK. Structural and functional classes of multipolar cells in the ventral cochlear nucleus. Anat Rec A Discov Mol Cell Evol Biol. 2006;288: 331–344.

3. Huang CG, Chacron MJ. Optimized parallel coding of second-order stimulus features by heterogeneous neural populations. J Neurosci. 2016;36: 9859–9872.

4. Ashida G, Heinermann HT, Kretzberg J. Neuronal population model of globular bushy cells covering unit-to-unit variability. PLoS Comput Biol. 2019;15: e1007563.

5. Nagayama S, Takahashi YK, Yoshihara Y, Mori K. Mitral and tufted cells differ in the decoding manner of odor maps in the rat olfactory bulb. J Neurophysiol. 2004;91: 2532–2540.

6. Borst JGG, Soria van Hoeve J. The calyx of Held synapse: from model synapse to auditory relay. Annu Rev Physiol. 2012;74: 199–224.

7. Englitz B, Tolnai S, Typlt M, Jost J, Rübsamen R. Reliability of synaptic transmission at the synapses of held in vivo under acoustic stimulation. PLoS One. 2009;4: e7014.

8. von Gersdorff H, Borst JGG. Short-term plasticity at the calyx of Held. Nat Rev Neurosci. 2002;3: 53–64.

9. Schneggenburger R, Forsythe ID. The calyx of Held. Cell Tissue Res. 2006;326: 311–337.

10. Smith PH, Joris PXPXPX, Yin TCTTCT, J.oris PX. Anatomy and physiology of principal cells of the medial nucleus of the trapezoid body (MNTB) of the cat. J Neurophysiol. 1998;79: 3127–3142.

11. Spirou GA, Brownell WE, Zidanic M. Recordings from cat trapezoid body and HRP labeling of globular bushy cell axons. J Neurophysiol. 1990;63: 1169–1190.

12. Xie R, Manis PB. Radiate and planar multipolar neurons of the mouse anteroventral cochlear nucleus: Intrinsic excitability and characterization of their auditory nerve input. Front Neural Circuits. 2017;11: 77.

13. Kreeger LJ, Honnuraiah S, Maeker S, Shea S, Fishell G, Goodrich L. An anatomical and physiological basis for flexible coincidence detection in the auditory system. Elife. 2025;13. doi:10.7554/elife.100492.3

14. Cao X-J, Oertel D. Auditory nerve fibers excite targets through synapses that vary in convergence, strength, and short-term plasticity. J Neurophysiol. 2010;104: 2308–2320.

15. McGinley MJ, Liberman MC, Bal R, Oertel D. Generating synchrony from the asynchronous: compensation for cochlear traveling wave delays by the dendrites of individual brainstem neurons. J Neurosci. 2012;32: 9301–9311.

16. Oertel D. The role of timing in the brain stem auditory nuclei of vertebrates. Annu Rev Physiol. 1999;61: 497–519.

17. Calkins DJ, Schein SJ, Tsukamoto Y, Sterling P. M and L cones in macaque fovea connect to midget ganglion cells by different numbers of excitatory synapses. Nature. 1994;371: 70–72.

18. Kolb H, Marshak D. The midget pathways of the primate retina. Doc Ophthalmol. 2003;106: 67–81.

19. Jacoby RA, Wiechmann AF, Amara SG, Leighton BH, Marshak DW. Diffuse bipolar cells provide input to OFF parasol ganglion cells in the macaque retina. J Comp Neurol. 2000;416: 6–18.

20. Köppl C. Auditory nerve terminals in the cochlear nucleus magnocellularis: differences between low and high frequencies. J Comp Neurol. 1994;339: 438–446.

21. Fukui I, Ohmori H. Tonotopic gradients of membrane and synaptic properties for neurons of the chicken nucleus magnocellularis. J Neurosci. 2004;24: 7514–7523.

22. Wolff M, Morceau S, Folkard R, Martin-Cortecero J, Groh A. A thalamic bridge from sensory perception to cognition. Neurosci Biobehav Rev. 2021;120: 222–235.

23. Sherman SM, Guillery RW. On the actions that one nerve cell can have on another: distinguishing “drivers” from “modulators.” Proc Natl Acad Sci U S A. 1998;95: 7121–7126.

24. Govindaiah G, Fox MA, Guido W. Pattern of driver-like input onto neurons of the mouse ventral lateral geniculate nucleus. eNeuro. 2023;10: ENEURO.0386-22.2022.

25. Rouiller EM, Welker E. A comparative analysis of the morphology of corticothalamic projections in mammals. Brain Res Bull. 2000;53: 727–741.

26. Groh A, de Kock CPJ, Wimmer VC, Sakmann B, Kuner T. Driver or coincidence detector: modal switch of a corticothalamic giant synapse controlled by spontaneous activity and short-term depression. J Neurosci. 2008;28: 9652–9663.

27. Buchholz MO, Gastone Guilabert A, Ehret B, Schuhknecht GFP. How synaptic strength, short-term plasticity, and input synchrony contribute to neuronal spike output. PLoS Comput Biol. 2023;19: e1011046.

28. Wu S, Wardak A, Khan MM, Chen CH, Regehr WG. Implications of variable synaptic weights for rate and temporal coding of cerebellar outputs. Elife. 2024;13: 1–26.

29. Osen KK. Cytoarchitecture of the cochlear nuclei in the cat. J Comp Neurol. 1969;136: 453–484.

30. Cant NB, Morest DK. Organization of the neurons in the anterior division of the anteroventral cochlear nucleus of the cat. Light-microscopic observations. Neuroscience. 1979;4: 1909–1923.

31. Spirou GA, Kersting MG, Carr S, Razzaq B, Alves-Pinto CY, Dawson M, et al. High-resolution volumetric imaging constrains compartmental models to explore synaptic integration and temporal processing by cochlear nucleus globular bushy cells. Elife. 2023;12: 1–44.

32. Liberman MC. Central projections of auditory-nerve fibers of differing spontaneous rate. I. Anteroventral cochlear nucleus. J Comp Neurol. 1991;313: 240–258.

33. Ostapoff EM, Morest DK. Synaptic organization of globular bushy cells in the ventral cochlear nucleus of the cat: a quantitative study. J Comp Neurol. 1991;314: 598–613.

34. Spirou GA, Rager J, Manis PB. Convergence of auditory-nerve fiber projections onto globular bushy cells. Neuroscience. 2005;136: 843–863.

35. Tolbert LP, Morest DK. The neuronal architecture of the anteroventral cochlear nucleus of the cat in the region of the cochlear nerve root: electron microscopy. Neuroscience. 1982;7: 3053–3067.

36. Joris PX, Carney LH, Smith PH, Yin TC. Enhancement of neural synchronization in the anteroventral cochlear nucleus. I. Responses to tones at the characteristic frequency. J Neurophysiol. 1994;71: 1022–1036.

37. Wei L, Karino S, Verschooten E, Joris PX. Enhancement of phase-locking in rodents. I. An axonal recording study in gerbil. J Neurophysiol. 2017;118: 2009–2023.

38. Nicol MJ, Walmsley B. Ultrastructural basis of synaptic transmission between endbulbs of Held and bushy cells in the rat cochlear nucleus. J Physiol. 2002;539: 713–723.

39. Wei L, Verschooten E, Joris PX. Enhancement of phase-locking in rodents. II. An axonal recording study in chinchilla. J Neurophysiol. 2023;130: 751–767.

40. Bruce IC, Erfani Y, Zilany MSA. A phenomenological model of the synapse between the inner hair cell and auditory nerve: Implications of limited neurotransmitter release sites. Hear Res. 2018;360: 40–54.

41. Goldberg JM, Brown PB. Response of binaural neurons of dog superior olivary complex to dichotic tonal stimuli: some physiological mechanisms of sound localization. J Neurophysiol. 1969;32: 613–636.

42. Johnson DHH. The relationship between spike rate and synchrony in responses of auditory-nerve fibers to single tones. J Acoust Soc Am. 1980;68: 1115–1122.

43. Heeringa AN. Single-unit data for sensory neuroscience: Responses from the auditory nerve of young-adult and aging gerbils. Sci Data. 2024;11: 1–13.

44. Heeringa AN, Zhang L, Ashida G, Beutelmann R, Steenken F, Köppl C. Temporal Coding of Single Auditory Nerve Fibers Is Not Degraded in Aging Gerbils. J Neurosci. 2020;40: 343–354.

45. Palmer a. R, Russell IJ. Phase-locking in the cochlear nerve of the guinea-pig and its relation to the receptor potential of inner hair-cells. Hear Res. 1986;24: 1–15.

46. Britt R, Starr A. Synaptic events and discharge patterns of cochlear nucleus cells. I. Steady-frequency tone bursts. J Neurophysiol. 1976;39: 162–178.

47. Smith PH, J.oris PX, Carney LH, Yin TCT, Joris PX. Projections of physiologically characterized globular bushy cell axons from the cochlear nucleus of the cat. J Comp Neurol. 1991;304: 387–407.

48. Smith PH, Rhode WS. Characterization of HRP-labeled globular bushy cells in the cat anteroventral cochlear nucleus. J Comp Neurol. 1987;266: 360–375.

49. Chase SM, Young ED. First-spike latency information in single neurons increases when referenced to population onset. Proc Natl Acad Sci U S A. 2007;104: 5175–5180.

50. Joris PX, Schreiner CE, Rees A. Neural processing of amplitude-modulated sounds. Physiol Rev. 2004;84: 541–577.

51. Van Tasell DJ, Soli SD, Kirby VM, Widin GP. Speech waveform envelope cues for consonant recognition. J Acoust Soc Am. 1987;82: 1152–1161.

52. Drullman R, Festen JM, Houtgast T. Effect of temporal modulation reduction on spectral contrasts in speech. J Acoust Soc Am. 1996;99: 2358–2364.

53. Rhode WS, Greenberg S. Encoding of amplitude modulation in the cochlear nucleus of the cat. J Neurophysiol. 1994;71: 1797–1825.

54. Wang X, Sachs MB. Neural encoding of single-formant stimuli in the cat. II. Responses of anteroventral cochlear nucleus units. J Neurophysiol. 1994;71: 59–78.

55. Palmer AR, Winter IM, Darwin CJ. The representation of steady-state vowel sounds in the temporal discharge patterns of the guinea pig cochlear nerve and primarylike cochlear nucleus neurons. J Acoust Soc Am. 1986;79: 100–113.

56. Smith RL, Brachman ML. Response modulation of auditory-nerve fibers by AM stimuli: effects of average intensity. Hear Res. 1980;2: 123–133.

57. Joris PX, Yin TC. Responses to amplitude-modulated tones in the auditory nerve of the cat. J Acoust Soc Am. 1992;91: 215–232.

58. Joris PX, Louage DH, Cardoen L, van der Heijden M. Correlation index: a new metric to quantify temporal coding. Hear Res. 2006;216–217: 19–30.

59. Kessler D, Carr CE, Kretzberg J, Ashida G. Theoretical relationship between two measures of spike synchrony: Correlation index and vector strength. Front Neurosci. 2021;15: 761826.

60. Joris PX, Smith PH. The volley theory and the spherical cell puzzle. Neuroscience. 2008;154: 65–76.

61. Rothman JSS, Young EDD. Enhancement of neural synchronization in computational models of ventral cochlear nucleus bushy cells. Aud Neurosci. 1996;2: 47–62.

62. Koert E, Kuenzel T. Small dendritic synapses enhance temporal coding in a model of cochlear nucleus bushy cells. J Neurophysiol. 2021;125: 915–937.

63. Keine C, Englitz B. Cellular and synaptic specializations for sub-millisecond precision in the mammalian auditory brainstem. Front Cell Neurosci. 2025;19: 1568506.

64. Oertel D. Synaptic responses and electrical properties of cells in brain slices of the mouse anteroventral cochlear nucleus. J Neurosci. 1983;3: 2043–2053.

65. Manis PB, Marx SO. Outward currents in isolated ventral cochlear nucleus neurons. J Neurosci. 1991;11: 2865–2880.

66. Reyes AD, Rubel EW, Spain WJ. Membrane properties underlying the firing of neurons in the avian cochlear nucleus. J Neurosci. 1994;14: 5352–5364.

67. Rothman JS, Young ED, Manis PB. Convergence of auditory nerve fibers onto bushy cells in the ventral cochlear nucleus: implications of a computational model. J Neurophysiol. 1993;70: 2562–2583.

68. Xu-Friedman MA, Regehr WG. Dynamic-clamp analysis of the effects of convergence on spike timing. I. Many synaptic inputs. J Neurophysiol. 2005;94: 2512–2525.

69. Rhode WS, Smith PH. Encoding timing and intensity in the ventral cochlear nucleus of the cat. J Neurophysiol. 1986;56: 261–286.

70. Huang C, Resnik A, Celikel T, Englitz B. Adaptive Spike Threshold Enables Robust and Temporally Precise Neuronal Encoding. Bethge M, editor. PLoS Comput Biol. 2016;12: e1004984.

71. Fontaine B, Peña JL, Brette R. Spike-threshold adaptation predicted by membrane potential dynamics in vivo. PLoS Comput Biol. 2014;10: e1003560.

72. Mittring A, Moser T, Huet AT. Graded optogenetic activation of the auditory pathway for hearing restoration. Brain Stimul. 2023;16: 466–483.

73. Strenzke N, Chanda S, Kopp-Scheinpflug C, Khimich D, Reim K, Bulankina AV, et al. Complexin-I is required for high-fidelity transmission at the endbulb of Held auditory synapse. J Neurosci. 2009;29: 7991–8004.

74. Wang H-P, Garcia JW, Sabottke CF, Spencer DJ, Sejnowski TJ. Feedforward thalamocortical connectivity preserves stimulus timing information in sensory pathways. J Neurosci. 2019;39: 7674–7688.

75. Kawasaki M, Rose G, Heiligenberg W. Temporal hyperacuity in single neurons of electric fish. Nature. 1988;336: 173–176.

76. Moore MJ, Caspary DM. Strychnine blocks binaural inhibition in lateral superior olivary neurons. J Neurosci. 1983;3: 237–242.

77. Wenthold RJ, Huie D, Altschuler R a., Reeks K a. Glycine immunoreactivity localized in the cochlear nucleus and superior olivary complex. Neuroscience. 1987;22: 897–912.

78. Wu SH, Kelly JB. Response of neurons in the lateral superior olive and medial nucleus of the trapezoid body to repetitive stimulation: Intracellular and extracellular recordings from mouse brain slice. Hear Res. 1993;68: 189–201.

79. Spangler KM, Warr WB, Henkel CK. The projections of principal cells of the medial nucleus of the trapezoid body in the cat. J Comp Neurol. 1985;238: 249–262.

80. Sommer I, Lingenhöhl K, Friauf E. Principal cells of the rat medial nucleus of the trapezoid body: an intracellular in vivo study of their physiology and morphology. Exp Brain Res. 1993; 223–239.

81. Srinivasan G, Friauf E, Löhrke S. Functional glutamatergic and glycinergic inputs to several superior olivary nuclei of the rat revealed by optical imaging. Neuroscience. 2004;128: 617–634.

82. Kopp-Scheinpflug C, Tozer AJB, Robinson SW, Tempel BL, Hennig MH, Forsythe ID. The sound of silence: ionic mechanisms encoding sound termination. Neuron. 2011;71: 911–925.

83. Grothe B, Pecka M, McAlpine D. Mechanisms of sound localization in mammals. Physiol Rev. 2010;90: 983–1012.

84. Yin TC, Chan JC. Interaural time sensitivity in medial superior olive of cat. J Neurophysiol. 1990;64: 465–488.

85. Tollin DJ, Yin TCT. Interaural phase and level difference sensitivity in low-frequency neurons in the lateral superior olive. J Neurosci. 2005;25: 10648–10657.

86. Friauf E, Ostwald J. Divergent projections of physiologically characterized rat ventral cochlear nucleus neurons as shown by intra-axonal injection of horseradish peroxidase. Exp Brain Res. 1988;73: 263–284.

87. Kuwabara N, DiCaprio RA, Zook JM. Afferents to the medial nucleus of the trapezoid body and their collateral projections. J Comp Neurol. 1991;314: 684–706.

88. Grande G, Wang L-Y. Morphological and functional continuum underlying heterogeneity in the spiking fidelity at the calyx of Held synapse in vitro. J Neurosci. 2011;31: 13386–13399.

89. Fekete A, Nakamura Y, Yang Y-M, Herlitze S, Mark MD, DiGregorio DA, et al. Underpinning heterogeneity in synaptic transmission by presynaptic ensembles of distinct morphological modules. Nat Commun. 2019;10: 826.

90. Chan RJ, Wang L-Y. Input-specific organization of intrinsic excitability expands coding capacity of fast-spiking auditory neurons. J Neurosci. 2025; e2305242025.

91. Wong NF, Brongo SE, Forero EA, Sun S, Cook CJ, Lauer AM, et al. Convergence of type 1 spiral ganglion neuron subtypes onto principal neurons of the anteroventral cochlear nucleus. J Neurosci. 2025;45: e1507242024.

92. Wang M, Zhang C, Lin S, Wang Y, Seicol BJ, Ariss RW, et al. Biased auditory nerve central synaptopathy is associated with age-related hearing loss. J Physiol. 2021;599: 1833–1854.

93. Sento S, Ryugo DK. Endbulbs of held and spherical bushy cells in cats: morphological correlates with physiological properties. J Comp Neurol. 1989;280: 553–562.

94. Rouiller EM, Cronin-Schreiber R, Fekete DM, Ryugo DK. The central projections of intracellularly labeled auditory nerve fibers in cats: an analysis of terminal morphology. J Comp Neurol. 1986;249: 261–278.

95. Yang H, Xu-Friedman M a. Emergence of coordinated plasticity in the cochlear nucleus and cerebellum. J Neurosci. 2012;32: 7862–7868.

96. Yang H, Xu-Friedman MA. Impact of synaptic depression on spike timing at the endbulb of Held. J Neurophysiol. 2009;102: 1699–1710.

97. Carney LH. Sensitivities of cells in anteroventral cochlear nucleus of cat to spatiotemporal discharge patterns across primary afferents. J Neurophysiol. 1990;64: 437–456.

98. Wang GI, Delgutte B. Sensitivity of cochlear nucleus neurons to spatio-temporal changes in auditory nerve activity. J Neurophysiol. 2012;108: 3172–3195.

99. Ngodup T, Goetz JA, McGuire BC, Sun W, Lauer AM, Xu-Friedman MA. Activity-dependent, homeostatic regulation of neurotransmitter release from auditory nerve fibers. Proc Natl Acad Sci U S A. 2015;112: 6479–6484.

100. Wong NF, Xu-Friedman MA. Time course of activity-dependent changes in auditory nerve synapses reveals multiple underlying cellular mechanisms. J Neurosci. 2022;42: 2492–2502.

101. Zhuang X, Sun W, Xu-Friedman MA. Changes in Properties of Auditory Nerve Synapses following Conductive Hearing Loss. J Neurosci. 2017;37: 323–332.

102. Helfert RH, Krenning J, Wilson TS, Hughes LF. Age-related synaptic changes in the anteroventral cochlear nucleus of Fischer-344 rats. Hear Res. 2003;183: 18–28.

103. McGuire B, Fiorillo B, Ryugo DK, Lauer AM. Auditory nerve synapses persist in ventral cochlear nucleus long after loss of acoustic input in mice with early-onset progressive hearing loss. Brain Res. 2015;1605: 22–30.

104. Gómez-Nieto R, Rubio ME. A bushy cell network in the rat ventral cochlear nucleus. J Comp Neurol. 2009;516: 241–263.

105. Häusser M, Mel B. Dendrites: bug or feature? Curr Opin Neurobiol. 2003;13: 372–383.

106. Keine C, Rübsamen R, Englitz B. Inhibition in the auditory brainstem enhances signal representation and regulates gain in complex acoustic environments. Elife. 2016;5: 19295.

107. Keine C, Rübsamen R. Inhibition shapes acoustic responsiveness in spherical bushy cells. J Neurosci. 2015;35: 8579–8592.

108. Keine C, Rübsamen R, Englitz B. Signal integration at spherical bushy cells enhances representation of temporal structure but limits its range. Elife. 2017;6: 29639.

109. Kopp-Scheinpflug C, Dehmel S, Dörrscheidt GJ, Rübsamen R. Interaction of excitation and inhibition in anteroventral cochlear nucleus neurons that receive large endbulb synaptic endings. J Neurosci. 2002;22: 11004–11018.

110. Nerlich J, Kuenzel T, Keine C, Korenic A, Rübsamen R, Milenkovic I. Dynamic fidelity control to the central auditory system: synergistic glycine/GABAergic inhibition in the cochlear nucleus. J Neurosci. 2014;34: 11604–11620.

111. Goyer D, Kurth S, Gillet C, Keine C, Rübsamen R, Kuenzel T. Slow cholinergic modulation of spike

probability in ultra-fast time-coding sensory neurons. eNeuro. 2016;3. doi:10.1523/ENEURO.0186-16.2016

112. Dehmel S, Kopp-Scheinpflug C, Weick M, Dörrscheidt GJGJ, Rübsamen R. Transmission of phase-coupling accuracy from the auditory nerve to spherical bushy cells in the Mongolian gerbil. Hear Res. 2010;268: 234–249.

113. Kuenzel T. Modulatory influences on time-coding neurons in the ventral cochlear nucleus. Hear Res. 2019;384: 107824.

114. Parker D. Variable properties in a single class of excitatory spinal synapse. J Neurosci. 2003;23: 3154–3163.

115. Sherman SM, Guillery RW. Distinct functions for direct and transthalamic corticocortical connections. J Neurophysiol. 2011;106: 1068–1077.

116. Özçete ÖD, Moser T. A sensory cell diversifies its output by varying Ca2+ influx-release coupling among active zones. EMBO J. 2021;40: e106010.

117. Chabrol FP, Arenz A, Wiechert MT, Margrie TW, DiGregorio D a. Synaptic diversity enables temporal coding of coincident multisensory inputs in single neurons. Nat Neurosci. 2015;18: 718–727.

118. Yates JL, Scholl B. Unraveling functional diversity of cortical synaptic architecture through the lens of population coding. Front Synaptic Neurosci. 2022;14: 888214.

119. Duarte R, Morrison A. Leveraging heterogeneity for neural computation with fading memory in layer 2/3 cortical microcircuits. PLoS Comput Biol. 2019;15: e1006781.

120. Sachdeva PS, Livezey JA, DeWeese MR. Heterogeneous synaptic weighting improves neural coding in the presence of common noise. Neural Comput. 2020;32: 1239–1276.

121. Perez-Nieves N, Leung VCH, Dragotti PL, Goodman DFM. Neural heterogeneity promotes robust learning. Nat Commun. 2021;12: 5791.

122. Tripathy SJ, Padmanabhan K, Gerkin RC, Urban NN. Intermediate intrinsic diversity enhances neural population coding. Proc Natl Acad Sci U S A. 2013;110: 8248–8253.

123. Huet A, Batrel C, Tang Y, Desmadryl G, Wang J, Puel J-L, et al. Sound coding in the auditory nerve of gerbils. Hear Res. 2016;338: 32–39.

124. Heeringa AN, Teske F, Ashida G, Köppl C. Cochlear aging disrupts the correlation between spontaneous rate and sound-level coding in auditory nerve fibers. J Neurophysiol. 2023;130: 736–750.

125. Versteegh CPC, Meenderink SWF, van der Heijden M. Response characteristics in the apex of the gerbil cochlea studied through auditory nerve recordings. J Assoc Res Otolaryngol. 2011;12: 301–316.

126. Hermann J, Pecka M, Von Gersdorff H, Grothe B, Klug A. Synaptic transmission at the calyx of held under in vivo-like activity levels. J Neurophysiol. 2007;98: 807–820.

127. Kanold PO, Davis KA, Young ED. Somatosensory context alters auditory responses in the cochlear nucleus. J Neurophysiol. 2011;105: 1063–1070.

128. Siveke I, Leibold C, Schiller E, Grothe B. Adaptation of binaural processing in the adult brainstem induced by ambient noise. J Neurosci. 2012;32: 462–473.

129. Yang Y, Adowski T, Ramamurthy B, Neef A, Xu-Friedman MA. High-speed dynamic-clamp interface. J Neurophysiol. 2015;113: 2713–2720.

130. Xu-Friedman MA, Regehr WG. Dynamic-clamp analysis of the effects of convergence on spike timing. II. Few synaptic inputs. J Neurophysiol. 2005;94: 2526–2534.

131. Bonferroni CE. Teoria statistica delle classi e calcolo delle probabilità. Pubblicazioni del R Istituto Superiore di Scienze Economiche e Commerciali di Firenze. 1936;8: 3–62.

132. Spearman C. The Proof and Measurement of Association between Two Things. Am J Psychol. 1904;15: 72.

133. Tolnai S, Englitz B, Kopp-Scheinpflug C, Dehmel S, Jost J, Rübsamen R. Dynamic coupling of excitatory and inhibitory responses in the medial nucleus of the trapezoid body. Eur J Neurosci. 2008;27: 3191–3204.

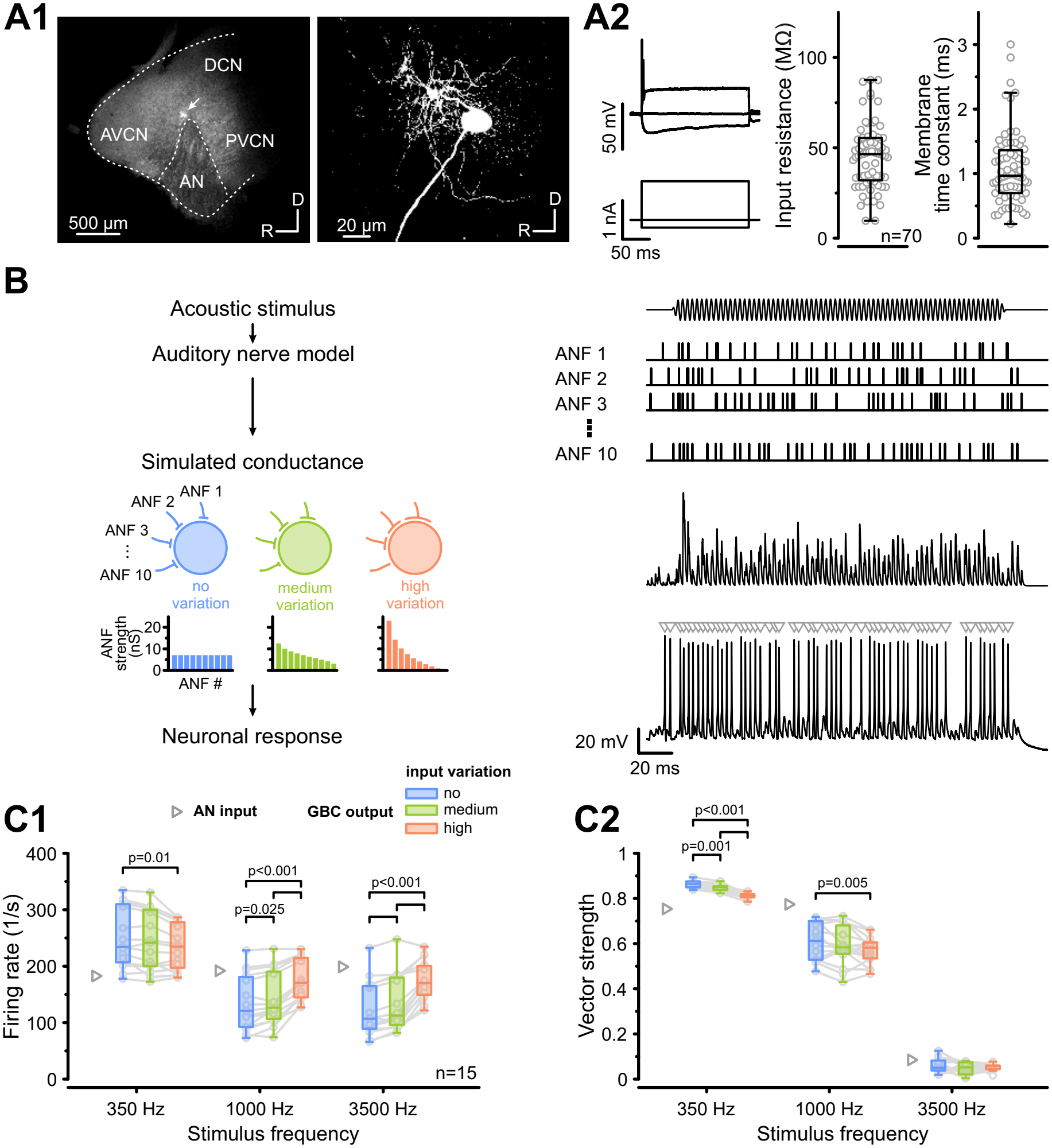
A1
DCN
AVCN
PVCN
AN
500 µm
D
R
20 µm
A2
50 mV
1 nA
50 ms
Input resistance (MΩ)
100
50
0
n=70
Membrane time constant (ms)
3
2
1
0
B
Acoustic stimulus
Auditory nerve model
Simulated conductance
ANF 1
ANF 2
ANF 3
ANF 10
no variation
medium variation
high variation
ANF strength (nS)
20
10
0
ANF #
Neuronal response
ANF 1
ANF 2
ANF 3
ANF 10
20 mV
20 ms
C1
AN input
GBC output
input variation
no
medium
high
Firing rate (1/s)
400
300
200
100
0
p=0.01
p<0.001
p=0.025
p<0.001
n=15
350 Hz
1000 Hz
3500 Hz
Stimulus frequency
C2
p<0.001
p=0.001
p=0.005
Vector strength
1
0.8
0.6
0.4
0.2
0
350 Hz
1000 Hz
3500 Hz
Stimulus frequency

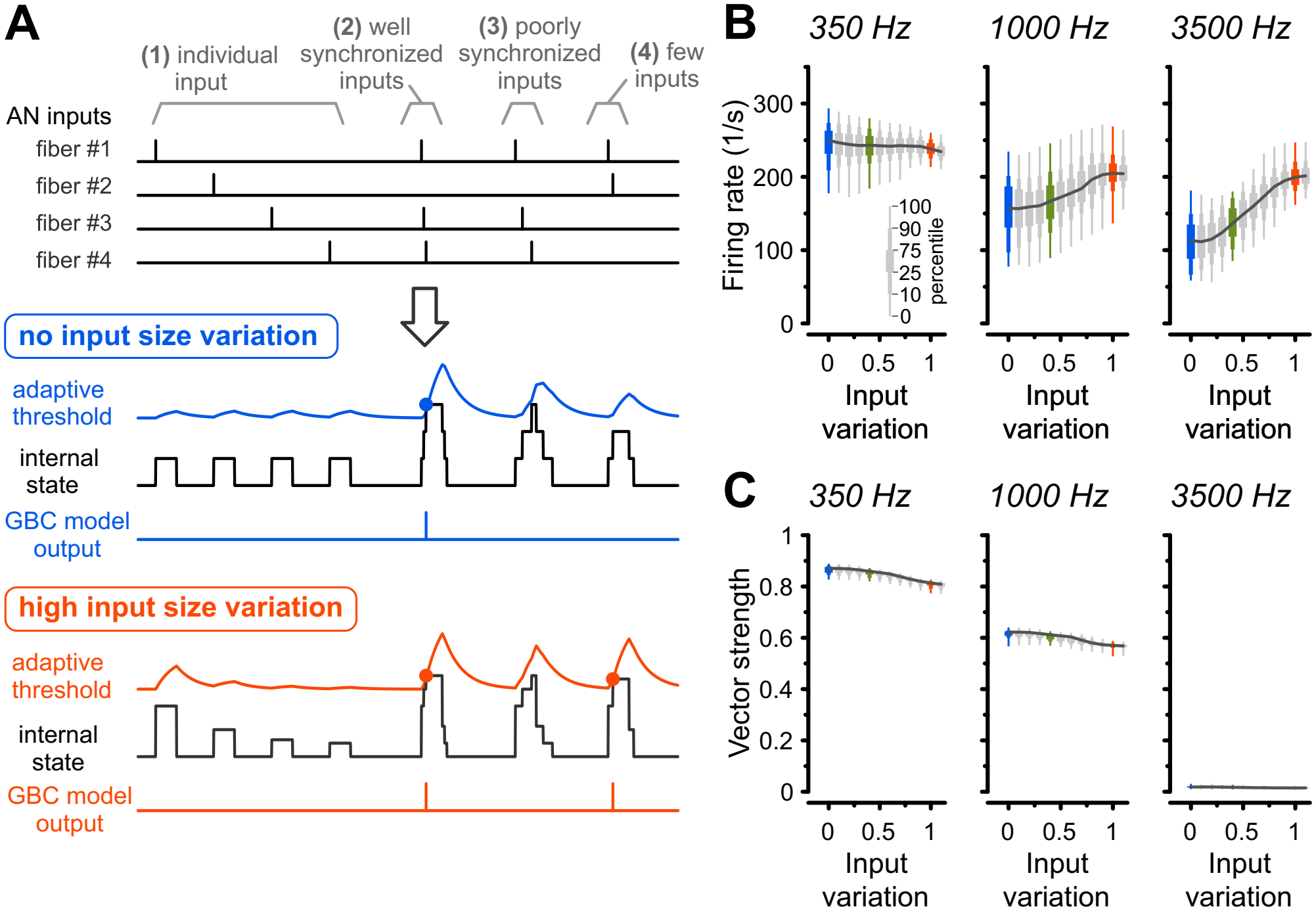
A
(1) individual input
(2) well synchronized inputs
(3) poorly synchronized inputs
(4) few inputs
AN inputs
fiber #1
fiber #2
fiber #3
fiber #4
no input size variation
adaptive threshold
internal state
GBC model output
high input size variation
adaptive threshold
internal state
GBC model output
B
350 Hz
1000 Hz
3500 Hz
Firing rate (1/s)
300
200
100
0
100
90
75
25
10
0
percentile
0
0.5
1
Input variation
C
350 Hz
1000 Hz
3500 Hz
Vector strength
1
0.8
0.6
0.4
0.2
0
0
0.5
1
Input variation

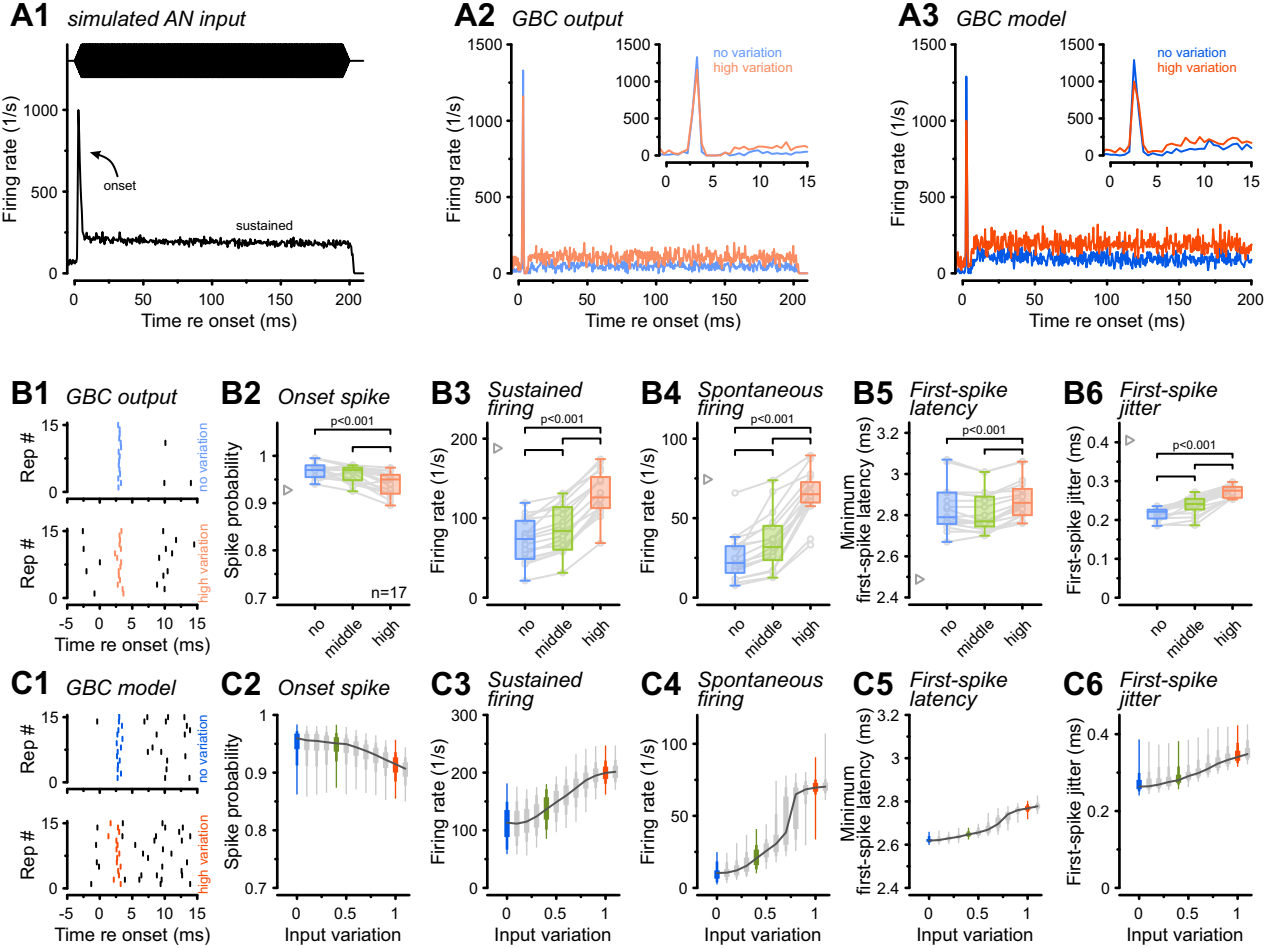
A1 simulated AN input
Firing rate (1/s)
onset
sustained
Time re onset (ms)
A2 GBC output
no variation
high variation
A3 GBC model
B1 GBC output
Rep #
no variation
high variation
Time re onset (ms)
B2 Onset spike
Spike probability
p<0.001
n=17
no
middle
high
B3 Sustained firing
Firing rate (1/s)
B4 Spontaneous firing
B5 First-spike latency
Minimum first-spike latency (ms)
B6 First-spike jitter
First-spike jitter (ms)
C1 GBC model
C2 Onset spike
C3 Sustained firing
C4 Spontaneous firing
C5 First-spike latency
C6 First-spike jitter
Input variation

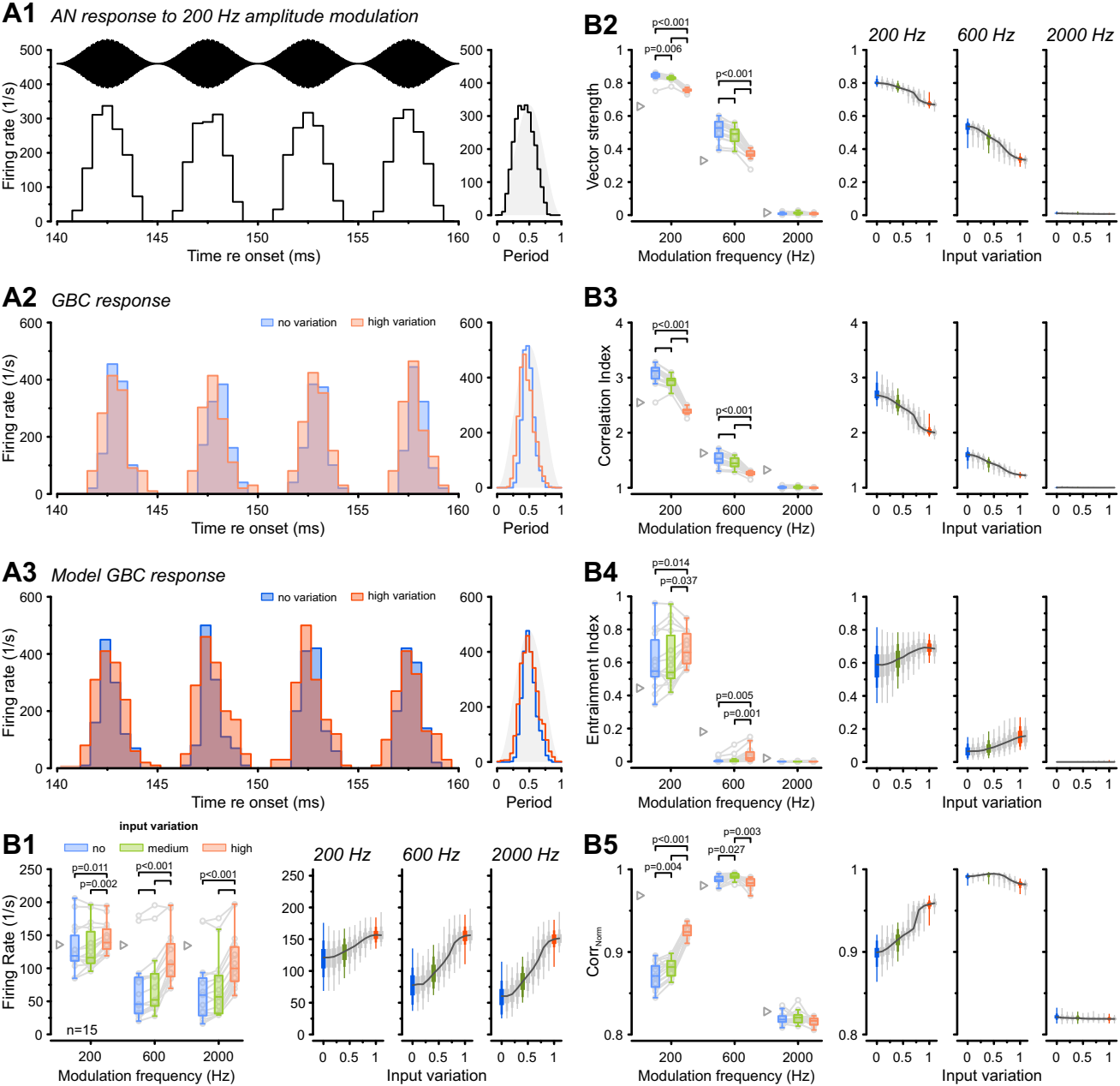
A1
AN response to 200 Hz amplitude modulation
Firing rate (1/s)
Time re onset (ms)
Period
B2
Vector strength
Modulation frequency (Hz)
Input variation
200 Hz
600 Hz
2000 Hz
p<0.001
p=0.006
A2
GBC response
no variation
high variation
B3
Correlation Index
A3
Model GBC response
B4
Entrainment Index
p=0.014
p=0.037
p=0.005
p=0.001
B1
input variation
no
medium
high
Firing Rate (1/s)
p=0.011
p=0.002
n=15
B5
Corr_Norm
p=0.004
p=0.027
p=0.003

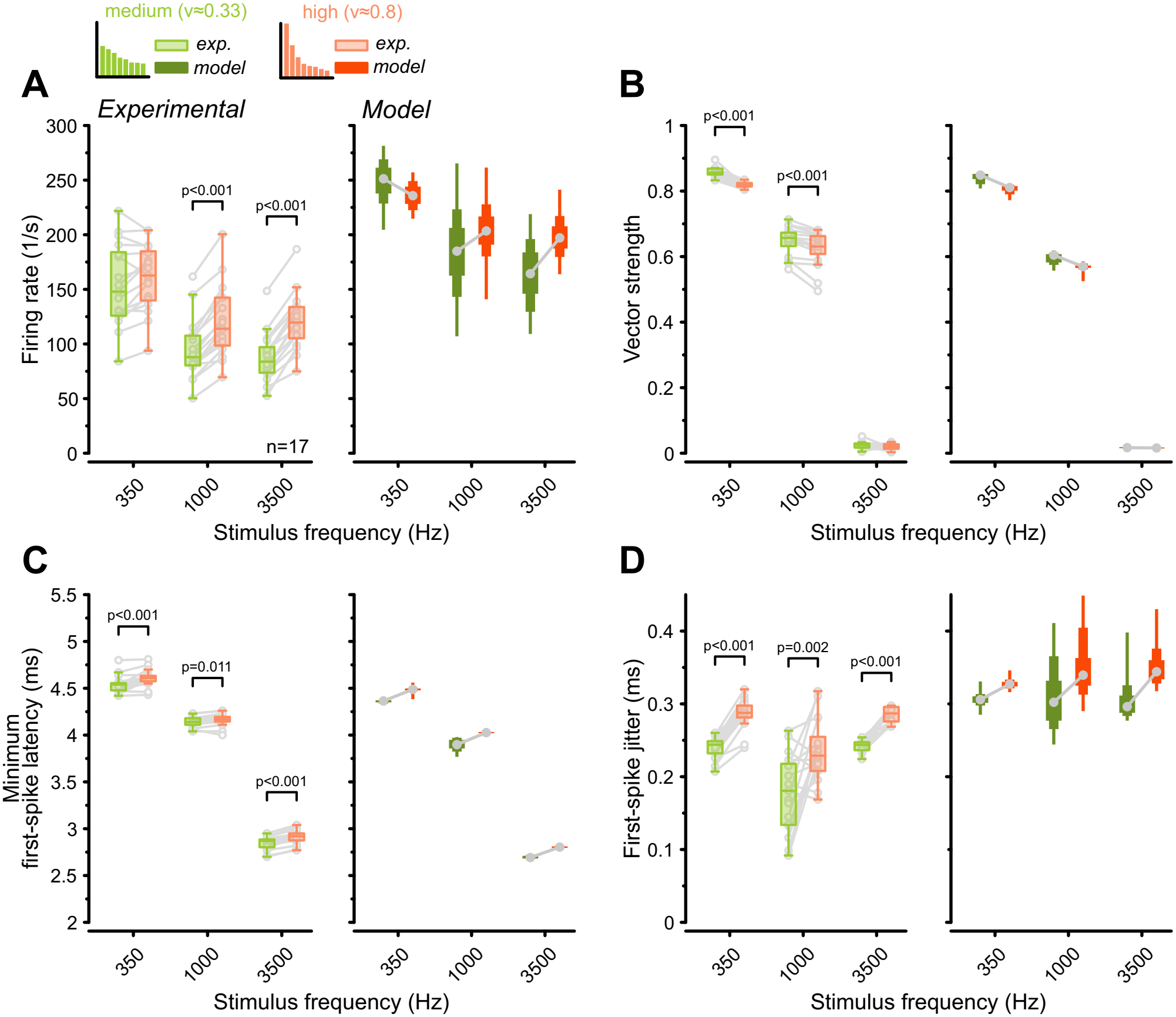
medium (v≈0.33)
exp.
model
high (v≈0.8)
exp.
model
A
Experimental
Model
Firing rate (1/s)
p<0.001
p<0.001
n=17
Stimulus frequency (Hz)
B
Vector strength
p<0.001
p<0.001
Stimulus frequency (Hz)
C
Minimum first-spike latency (ms)
p<0.001
p=0.011
p<0.001
Stimulus frequency (Hz)
D
First-spike jitter (ms)
p<0.001
p=0.002
p<0.001
Stimulus frequency (Hz)

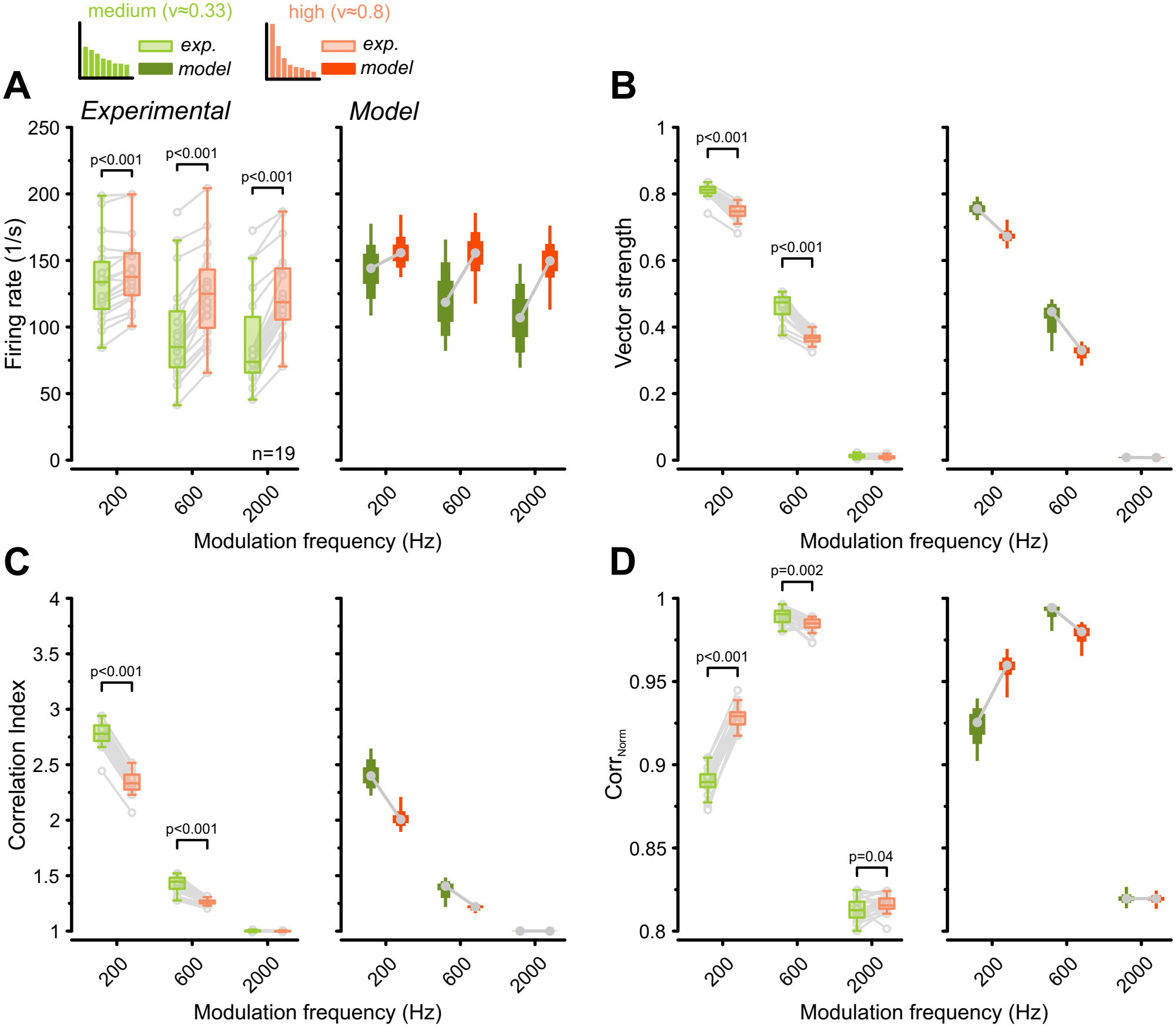
medium (v≈0.33)
high (v≈0.8)
exp.
model
exp.
model
A
Experimental
Model
Firing rate (1/s)
p<0.001
p<0.001
p<0.001
n=19
Modulation frequency (Hz)
B
Vector strength
p<0.001
p<0.001
Modulation frequency (Hz)
C
Correlation Index
p<0.001
p<0.001
Modulation frequency (Hz)
D
Corr_Norm
p=0.002
p<0.001
p=0.04
Modulation frequency (Hz)